68th Meeting of the AEROBALLISTIC RANGE ASSOCIATION
Monterey, CA, USA, September 17 – 23, 2017.

Upgrades and Modifications of the NASA Ames HFFAF Ballistic Range

David W. Bogdanoff*
AMA, Inc., Moffett Field, CA 94035

Michael C. Wilder†, Charles J. Cornelison‡
NASA-Ames Research Center, Moffett Field, CA 94035

Alfredo J. Perez§
Aerodyne Industries, Moffett Field, CA 94035

ABSTRACT

Recent developments at the NASA Ames Hypervelocity Free Flight Aerodynamic Facility (HFFAF) ballistic range are described, including the conversion of the shadowgraph stations from film-based cameras to digital cameras. The various configurations of the shadowgraph stations are presented, and resolution tests of film and two types of digital camera are described. Digital camera resolution of ~4000 x 4000 pixels nearly achieves film resolution. The advantages of the digital cameras are discussed, including the immediate availability of the shadowgraphs. Tests have been conducted to assess the applicability of a commercially-available model detection system. A new gunpowder, St. Marks Powder WC 886, was assessed for the NASA Ames 6.25"/1.50" light gas gun to replace the traditionally-used Hercules HC-33-FS powder, which is no longer available. The results from eight proof shots for the two powders are presented. Both muzzle velocities and piston velocities are 5 – 9% lower for the new St. Marks WC 886 powder than for the old Hercules HC-33-FS powder. Computed piston and muzzle velocities are in good agreement with experiment. Finally, shadowgraph-reading software that employs template-matching pattern recognition to locate the ballistic-range model is described. Templates are generated from a 3D solid model of the ballistic-range model. The accuracy of the approach is assessed using a set of computer-generated test images.

I. INTRODUCTION

The NASA Ames Hypervelocity Free Flight Aerodynamic Facility (HFFAF) ballistic range was initially developed to support the Apollo program, and since then nearly every blunt-body entry vehicle flown by NASA, from Apollo to Orion, Viking to Mars Science Laboratory (MSL), has been tested in the facility [1]. The HFFAF has also extensively supported fundamental studies of the fluid- and gas-dynamics of hypersonic flight.

The range has sixteen orthogonal shadowgraph stations located at 1.52 m intervals over a total length of 22.9 m. A total of 32 photographs are taken for each shot. A photo of the test section and the original horizontal shadowgraph cameras looking west is shown in Fig. 1. Figure 2 shows a corresponding view looking east. The range can be operated at pressures of 100 microns to one atmosphere and can be back-filled with various gases such as nitrogen, argon and carbon dioxide. The windows have diameters of 30 cm (first 9 stations) and 38 cm (later stations). A variety of powder guns and two-stage light gas guns is available to launch models. Powder guns with launch tube diameters ranging from 20 to 61 mm are available and can launch models with velocities

* Senior Research Scientist, AMA, Inc.
† Aerospace Engineer, Aerothermodynamics Branch.
‡ Facility Manager, Ballistic Range Complex, Thermo-Physics Facilities Branch.
§ Electronics Engineering Technician, Ballistic Range Complex, Thermo-Physics Facilities Branch.

of 170 m/sec to 2 km/sec. Two stage light gas guns with launch tube diameters of 7 to 38 mm are available and can launch models with velocities of 3 to 8 km/sec.

A number of upgrades and refurbishments to the HFFAF were performed in the 1990s and reported in Ref. 2. More recently, the development of new test capabilities and improved test techniques, and the deployment of improved instrumentation, have been reported [Refs. 3 - 6]. This paper will discuss the recent conversion of the 32 shadowgraph cameras from film to digital recording, recent experiments with an off-the-shelf system for model detection, evaluation of a new gunpowder for use in the light gas gun, and developments in image-reading software.

II. SHADOWGRAPH IMAGING

As mentioned in the introduction, the HFFAF is equipped with 16 shadowgraph imaging stations, each of which has two orthogonal imaging systems (side and top views). In the original setup images were recorded on photographic film, requiring 2 to 3 hours to process, which in turn meant a 2 to 3 hour delay in assessing the quality of a test. Additionally, each film set required several hours to digitize for analysis in the film-reading software. With the desire to improve testing productivity and to eliminate the need for maintaining a film-processing capability, experiments have been conducted over the past seven years with various digital imaging approaches. Initially, several stations were equipped with intensified charge-coupled device (ICCD) cameras previously employed in the NASA Ames Gun Development Facility [7]. More recently, the remaining stations have been equipped with digital single-lens reflex (SLR) cameras. The following sections will describe each system, and the resolution of each will be compared in section IID.

A. Original sheet film shadowgraph stations

A top view sketch of the optical set-up of one of the original horizontal shadowgraph stations is shown in Fig. 3. The spark gap, with a source diameter of ~1 mm and a light pulse duration of ~0.3 microsecond, is located on the left (north) side of the test section and illuminates a mirror with a focal length of 1.93 m. Figure 4 (from Ref. 8) shows radiated power as a function of wavelength for the spark gap, along with black body (BB) curves for 20,000 and 23,000 degrees K. The mirror produces a parallel beam of light which passes through the test section windows as shown. The mirror diameters (30 and 38 cm) match the window diameters. In Fig. 3, on the right (south) side of the test section, an identical mirror images the spark gap at the center of the Kerr cell and, at the same time, images the center of the test section on the film plane, where 20 cm x 25 cm sheets of film are placed. The most recent sheet film used was Ilford HPS Plus ISO 400, push-processed to ISO 3200. This film has a wavelength sensitivity range of ~360 to ~650 nm. The Kerr cell is an electro-optic crossed polarizer shutter with an open time of 40 ns. Figure 5 (from Ref. 9) shows the spectral transmissivity of the Kerr cell (parallel) polarizers and of the complete Kerr cell. It is noted that the transmission of the Kerr cell falls off steeply at ~310 nm. The Kerr cells are now operated with benzonitrile fill instead of the original nitrobenzene fill, since the benzonitrile is less toxic. Since the Kerr constant for the benzonitrile is less than that of the nitrobenzene, the Kerr cells are not completely open at the maximum Kerr cell voltage, but sufficient light is passed through for imaging. The Kerr cell shutter (open time = 40 ns) is used to freeze the motion of the hypervelocity models and to keep extraneous light from reaching the film. The extraneous light may arise from muzzle flash, impact flash and radiation from the bow shock and the wake of the projectile. Figure 6 shows an enlarged view of the final section of the optical path of Fig. 3, showing the Kerr cell and film plane.

Figure 7 shows a spark gap and a collimating mirror on the north side of the test section. Figure 8 shows a single station on the south side of the test section looking north. The red film box is in the center of the picture, with the film holder at the back (towards the test section) shown with the dark slide up, film ready for exposure. The Kerr cell is the white cube at the left of the Kerr cell assembly in the foreground. To the right of the Kerr cell, the blue and white box contains the pulse forming network (PFN) (above) and the switching hydrogen thyratron (below) used to initiate the 40 ns pulse for the Kerr cell. The PFN also emits a pulse used to stop the interval timer associated with that station, and located in the facility control room. The timers (one for each station) are all initiated by a common start pulse at gun fire, and stopped when the station's Kerr cell is triggered, thus providing the projectile flight time between each station. Figure 9 shows the corresponding view looking south. The red film box is in the foreground, hiding the Kerr cell assembly and the focusing mirror is in the background.

The discussion above and the figures referenced all refer to the horizontal shadowgraph set-ups. For each horizontal shadowgraph set-up, there is a corresponding vertical shadowgraph set-up. The optical trains for the horizontal and vertical shadowgraph set-ups are identical (e.g., see Fig. 3), only oriented differently. The spark gaps are on the top of the test section and the collimating mirrors are on the roof. The focusing mirrors are at the bottom of a trench under the test section. The Kerr cell assembly and the film box are also in the trench, 2 to 3 m above the mirrors.

B. Shadowgraph stations with ICCD cameras

The ICCD camera model in use is a Princeton Instruments/Acton PI-MAX2 intensified CCD camera with a 1024 x 1024 pixel array. This camera, which is typically used for low-light, high-temporal-resolution scientific imaging, uses a gated image intensifier, coupled to the CCD array, to achieve exposures as short as 2 ns. Since the ICCD camera can be gated, the Kerr cell shutter is unnecessary. The camera has a wavelength sensitivity range of ~500 to ~880 nm, which is at the high wavelength, low-intensity, end of the spark gap output (see Fig. 4). The intensification is sufficient, however, to use a gate time of 5 ns, which is more than sufficient to freeze the motion of hypervelocity models. An additional lens is required to image the center of the test section on the CCD sensor. An achromatic doublet lens is used to reduce on-axis spherical and chromatic aberrations, and the focal length was selected to capture the full diameter of the station window on the sensor. The facility model-detection signal that would ordinarily trigger the Kerr cell is used to trigger the gating of the ICCD camera; however, the high-voltage facility model-detection signal is first attenuated through a voltage divider to the levels (< 10 V) acceptable to the ICCD camera.

Figure 10 shows the final section of the shadowgraph optical path when an ICCD camera is used. Figure 10 corresponds to Fig. 6 for an original sheet film horizontal shadowgraph station. With the ICCD cameras, the remainder of the optical set-up from the spark gap to the Kerr cell location remains as shown in Fig. 3. Figure 11 shows a photograph of a single station on the south side of the test section, looking northeast. The camera, lens and Kerr cell assembly without the Kerr cell are visible. Figure 12 shows the corresponding view looking south. The focusing mirror is in the background.

One station was set up as shown in Fig. 11 in order to test the use of an ICCD camera for shadowgraph imaging. While the resolution of the ICCD cameras is lower than film (see Section IID), it is sufficient in most cases, particularly when used at vertical stations. The horizontal stations in the HFFAF are used to provide down-range position measurements of models, and typical aerodynamics tests are designed such that the pitch angle and vertical motion of the model, imaged from the horizontal stations, are the primary data of interest. As a consequence, lower image resolution in the vertical images can be tolerated, provided only a few stations are so equipped and that each ICCD camera station is preceded, and followed, by high resolution camera stations. Four vertical stations were initially converted to allow quick assessment of a test while the remaining film images were being processed. Currently, six vertical stations are equipped with ICCD cameras.

C. Shadowgraph stations with SLR cameras

In recent years a number of high-resolution, and relatively inexpensive, digital SLR cameras have become available. Results described here are for the Nikon D3200 SLR camera with a 4000 x 6000 pixel CMOS imaging array. The camera produces a color image in a red-green-blue (RGB) format. Only a monochrome image is required for a shadowgraph, and since the spark gap light source is brightest in the blue end of the spectrum (see Fig. 4), only the blue component of the image is retained. The cameras are operated between ISO 200 and 400, depending on the performance of the spark gap and Kerr cell at each station. Figure 13 shows the final section of the shadowgraph station optical path when an SLR camera is used. As with the ICCD camera, an achromatic lens is used to image the test section on the sensor, but the Kerr cell is required to shutter the camera (compare Fig. 10 for the ICCD camera and Fig. 6 for an original sheet film shadowgraph station). With the SLR cameras, as with the ICCD cameras, the remainder of the optical set-up from the spark gap to the Kerr cell remains as shown in Fig. 3. Figure 14 shows a photograph of a single station on the south side of the test section, looking north. The camera and Kerr cell assembly are visible. The imaging lens is located between the Kerr cell and the camera body within a fully-enclosed, light-tight assembly. Figure 15 shows the corresponding view, looking south. The focusing mirror is in the background. Figure 16 shows the array of the 16 horizontal SLR shadowgraph stations, looking west.

The SLR cameras are equipped with a mechanical shutter, which is too slow for ballistic-range photography, but which must be opened prior to firing, and closed after the shot. A controller unit was designed and built in-house to achieve this. The controller uses an OSEPP Pro microcontroller based on the open source Arduino Pro controller unit. The cameras are operated in bulb mode, with the shutter activated through the camera's remote-control port by mechanical relays in the Arduino camera control unit. When the gun is fired, the facility control panel provides a signal to energize the model-detection photo beam system. At the same time, the firing panel provides the Arduino with a signal to open the camera shutters. After a programmed delay, or when the camera trigger light sheets are de-energized and the Arduino has stopped receiving the signal from the facility, the camera shutters will close and the image will be stored on the camera's memory card. After the shot, the images are downloaded via a network of USB range extenders to a computer in the main control room. A manual trigger located on the Arduino housing can also be utilized for manual testing and troubleshooting the camera stations during alignment checks.

Currently, 26 out of 32 shadowgraph imaging systems are equipped with these SLR cameras and Kerr cell shutters. The remaining 6 systems (all vertical stations) are equipped with gated ICCD cameras described in the previous section.

D. Resolution tests of shadowgraph imaging methods

In order to assess the spatial resolution of each shadowgraph camera configuration, images of a USAF 1951 test chart were obtained, with the chart located on the centerline of the HFFAF ballistic range test section. Figure 17 shows an image taken at a station with a 30 cm diameter window, as well as the detail of the resolution chart starting at line group 0. Each line group has six elements, and each element comprises three vertical bars and three horizontal bars. The width and spacing of the bars decreases for each element and group, ranging from 0.5 mm (1 line/mm) for element 1 of group 0 to 0.14 mm (3.56 lines/mm) for element 6 of group 1, which are the line groups of interest here.

Figure 18 shows images of groups 0 and 1 of the test chart taken with each shadowgraph configuration. Figure 18(a) shows a high-resolution scan of a sheet film negative. When scanned at this resolution the film grain is nearly resolved and further increases in scan resolution are nearly indistinguishable. The resulting digital image of the full window diameter (as shown in Fig. 17) is ~3600 x 3600 pixels for the 30 cm diameter windows, and ~4500 x 4500 pixels for the 36 cm diameter windows. In terms of the number of pixels/cm of the physical object in the range, the resolution is ~120 pixels/cm for both. The object to film image magnification is ~0.5. Figure 18(b) shows the ICCD camera image of the chart. The focal length of the imaging lens used for the ICCD cameras gives a field of view ~26 cm across, slightly cropping the outer edges for both the 30 cm and 36 cm diameter windows, and resulting in an object resolution of ~38 pixels/cm. For the digital SLR cameras, an imaging lens focal length was selected such that the image of the shadowgraph station window approximately fills the height of the sensor (4000 pixels). As a result, the object resolution is slightly lower for the stations with the larger diameter windows. Figure 18(c) shows the digital SLR image at a station with a 30 cm diameter window, and Fig. 18(d) shows the digital SLR image at a station with a 38 cm diameter window. The object resolutions are ~130 pixels/cm and ~105 pixels/cm, respectively, which are approaching the ultimate resolution of the film grain. It can be seen from the test-chart images that the scanned film and the digital SLR images all resolve elements in group 1 to at least element 3, which has a line spacing of 2.52 lines/mm, and a line width of 0.198 mm. The ICCD resolution is closer to element 4 of group 0, which has a line spacing of 1.41 lines/mm, and a line width of 0.355 mm. These resolutions are summarized in Table 1.

Typical HFFAF models range from 15 mm to 38 mm in diameter, and a general rule of thumb for accurate attitude measurements is to have at least ~200 pixels on the long axis of the model (usually the diameter for models representing blunt-body atmospheric entry vehicles). Figure 19 shows shadowgraph images of a 33 mm diameter blunt cone in flight at 2700 m/s for each of the cameras discussed above. For this example, all three systems provide sufficient spatial resolution to determine the model attitude. It should be noted that for any recording method, the image quality can be expected to vary from shot to shot, and station to station, due to variations in the performance of spark gaps, cameras, and (when used) Kerr cells; variations in optical alignment; and, for film, from batch to batch variations in the development process. The images shown in Figs. 17-19 are nominal examples.

Table 1. Digital image sizes and object resolutions for the various shadowgraph imaging set-ups.

Camera Type	Field of View Diameter (cm)	Digital Image Size (pixels)*	Object Resolution (pixels/cm)*	USAF 1951 Test Chart Resolution	
				Bar Width (mm)	Line Spacing (lines/mm)
Film (high-resolution scan)	30	3600 x 3600	120	0.198	2.52
	38	4500 x 4500			
ICCD	26	1024 x 1024	38	0.355	1.41
Digital SLR	30	4000 x 4000	130	0.198	2.52
	38		105		

*Note: These are nominal values, actual values will vary slightly based on the actual image magnification at each station.

III. MODEL DETECTION

When the model reaches the center of a shadowgraph station window, it must trigger the firing of the spark gap light source and, after a delay of ~0.5 microsecond, the Kerr cell or camera gate. The delay is to allow the picture to be taken about at the maximum output of the spark gap. The heritage model detection system in the HFFAF was designed and built in the 1960's and employs vacuum-tube-based electronics for signal detection and conditioning. Maintenance requirements are relatively high for this system, and there is a risk that the necessary tubes will eventually become unavailable. A commercially-available, IR diode-based detection system was successfully employed in the NASA Ames Gun Development Facility for supersonic testing [7]. Three stations in the HFFAF were equipped with such units to evaluate their applicability in hypersonic testing when there is significant luminosity generated by the bow shock of the projectile.

A. Original visible light sheet trigger stations with halogen lamps and phototubes

An original shadowgraph light sheet trigger station is shown in the sketch of Fig. 20. The light source is a 6.6 A, 100 W tungsten halogen airfield lamp with a R7S base. The lamp is located below the test section as shown and a strip mirror creates a parallel light sheet which crosses the test section inclined at an angle of ~11 degrees. The light sheet covers almost all of the viewing area through the windows. After crossing the test section, the light sheet strikes a second strip mirror, above the test section, which focuses the light on to a Cetron 6570 phototube. The output of the phototube then passes to electronic triggering circuits which were originally programmed to fire on the light decrease due to the passage of the model. These circuits then provide output pulses to fire the spark gap and trigger the Kerr cell or the camera gate. To handle the cases of self-luminous models, the triggering circuits are currently set to trigger on either light decrease or light increase. Figure 21 shows a side view photograph of the trigger station. Figure 22 shows details of the upper components of the trigger station. Figure 23 shows the lower strip mirror and the halogen lamp housing of the trigger station.

B. Light sheet trigger stations with IR LEDs and IR phototransistors

It was decided to investigate an alternative shadowgraph light sheet trigger station using IR LEDs and IR phototransistors. This type of trigger station is shown in the sketch of Fig. 24. Compared to the original visible light trigger stations, the light source is an array of 72 IR LEDs instead of a halogen lamp and the detectors are an array of 7 IR phototransistors instead of a phototube. Note that the strip mirrors of the visible light trigger stations are not needed with the IR trigger stations. These trigger stations are constructed by dismantling an Oehler Research Model 57 infrared ballistic screen. The Oehler units are separated into two parts, permitting us to locate the IR emitters and detectors about 2.6 m apart, as shown in Fig. 24. Figure 25 shows a side view photograph of an IR trigger station. Figure 26 shows details of the upper components of the trigger station, including the phototransistors. Figure 27 shows the array of 72 IR LEDs below the test section. The IR light sheet trigger stations have been found to be somewhat more likely to trigger at erroneous times when used with self-luminous models than the original visible light sheet trigger stations. Efforts to spatially filter the light reaching the detectors, and to block light originating up-range, did not improve performance. Currently, the original system is required for speeds above ~3 km/s.

IV. REPLACEMENT GUNPOWDER FOR LIGHT GAS GUN OPERATIONS

For the NASA Ames 38 mm two stage light gas gun, the powder used for a number of years was Hercules HC-33-FS powder. This is a double base powder with 7.0% nitroglycerin and a cylindrical, 7-perforation grain with a web of 0.0635 cm. This powder is no longer available. After a certain amount of research, a replacement powder was located. It is the St. Marks WC 886 powder. This is a double base powder with 13.0% nitroglycerin and a flattened ball grain shape with a thickness of 0.0686 cm. These two powders are the only powders qualified for the US Army's 25 mm M791 APDS ammunition, meeting the velocity/pressure and action time requirements of the ammunition. Data for the two powders is given in Table 2.

Three proof shots were made with the new WC 886 powder with the NASA Ames 6.25"/1.50" light gas gun. The gun operating conditions were:

Gun had two 20 foot long lengths out of the total pump tube length of ~100 feet removed.
Powder mass = 1100, 1500 and 2000 g
Hydrogen pressure = 68. 3 psia
Piston mass = 21,300 g
Break valve rupture pressure = 3.2 ksi
Projectile = ~49 g Lexan slug
Range pressure = ~20 Torr

Table 2. Data for Hercules HC-33-FS and St. Marks WC 886 gunpowders.

Powder type		Hercules HC-33FS	St. Marks WC 886
Composition (%)			
	Nitrocellulose (NC)	Remainder	Remainder
	Nitrogen in NC	13.0	
	Nitroglycerin	7.0	13.0
	Diphenylamine	1.0	
	Potassium nitrate	1.0	
	Graphite (added)	0.3	
	Deterrent	2.0	6.5*
Dimensions (cm)			
	Length	0.33	0.0686
	Diameter	0.279	0.127
	Web	0.0635	0.0686†
	Perforations	7	0

*Added as an outer coating
†Taken equal to length (grain is a flattened ball)

In 2012, five corresponding proof shots were made with the HC-33-FS powder. The powder loads for these shots were 1100, 1300, 1500, 1750 and 2000 g. Except for some of the powder loads, all other parameters were the same for the two series of proof shots. Figures 28 and 29 show, as a function of powder load, the muzzle velocities and piston velocities, respectively, for the total of eight proof shots. It is seen that the muzzle velocities are 5 to 8% lower for the WC 886 powder than for the HC-33-FS powder. Correspondingly, the piston velocities are 5 to 9% lower for the WC 886 powder than for the HC-33-FS powder. The difference in performance of the powders can easily be compensated for by using powder loads with the new powder ~10% larger than those used with the old powder.

Figures 30 and 31 show experimental versus CFD muzzle velocities and piston velocities, respectively, for the eight proof shots. The CFD calculations were performed using a higher-order Godunov CFD code described in Refs. 10 and 11. The version of the code presented in Ref. 11 was used. The deterrent (used to slow down the linear burn rate of the powder) for the WC 886 powder is taken to be in the outer part of the grain and is

assumed to decrease from 4 x 6.5 = 26% at the grain surface to 0% halfway through the grain to the center (Ref. 12). Given the percentages of NC (nitrocellulose), NG (nitroglycerin) and deterrent [taken to be DBP (dibutyl phthalate)], the nominal burn rate equation can be calculated from the correlations of Ref. 13. Tuning the burn rate for the CFD code) resulted in a best fit burn rate of 0.88 times the nominal value. [Tuning the burn rate is always necessary, since the burn rates in the literature (which are for powder chamber pressures substantially higher than those used in two-stage light gas guns) are found not to correspond to actual burn rates observed with two stage guns.] The break valve rupture pressure has a nominal value of 3.2 ksi, which was used for the HC-33-FS calculations. For the WC 886 calculations, a break valve rupture pressure of 2.61 ksi was found to give a better agreement between theory and experiment. The actual rupture pressure for the break valve with dynamic pressure loading is not exactly known.

V. NEW HARDWARE FOR FACILITY SYSTEMS CHECKS

To check out the shadowgraph stations, a rifle mounted at the muzzle of the two stage light gas gun, is used. For many years, a 0.22 in (5.6 mm) caliber rifle, using 0.22 Swift ammunition, was used. It became increasingly harder to find the Swift ammunition, and hence, a shift to a 0.204 in (5.2 mm) Ruger rifle was made. The quoted muzzle velocities for the two rounds are almost identical, about 1286 m/s. This is for a 2.59 g Swift bullet and a 2.07 g Ruger bullet.

VI. IMAGE READING SOFTWARE DEVELOPMENTS

In aerodynamic testing the position and attitude of the ballistic-range models are measured relative to a fiducial wire system. Figure 32 shows an orthogonal pair of shadowgraph images captured at the first station in the HFFAF, and indicates the fiducial wires and the coordinate-system orientation. The catenary wires and taut wires are continuous wires running the full length of the test section. There is a complete set of wires on each side of the test section in both views, which are slightly offset from each other so both sets are imaged. All wires are located outside the test-section chamber. Down range, x, and vertical, z, positions of the model are measured relative to the crossing of the first pair of plumb and catenary wires in the side-view image (Fig. 32(a)). The pitch angle, θ, is measured relative to the plumb wire, with positive pitch in the nose-up attitude. The cross range, y, position is measured from the top-view image (Fig. 32(b)) relative to the first (top-most in the image) taut wire, and the yaw angle, ψ, relative to this wire, as shown. Scale factors relating image pixels to physical units are based on the known distances between plumb wires (horizontal image scales) and taut wires (vertical image scales).

The state of the art in image reading software employed in the HFFAF is the Comprehensive Automated Aerodynamic Reduction System for Ballistic Ranges, or CADRA [14]. CADRA determines the position and attitude of the model either from the weighted centroid of the pixels comprising the model, or by template matching. The current implementation of CADRA in use in the HFFAF develops templates from a 2D profile of the model, which is sufficient for models that are axially symmetric bodies of revolution, as are the models typically tested in the HFFAF. Recently, however, a test was conducted of a faceted model, shown in Fig. 33 from Ref. 15, whose 2D profile varies with attitude. The model represents the Adaptive Deployable Entry and Placement Technology (ADEPT) Sounding Rocket (SR-1) flight-test vehicle [16]. The model also featured a rectangular aft body, representing the CubeSat payload of the SR-1 vehicle. Because of this shape, the profile projected into the shadowgraph images (e.g., the length to diameter ratio) varies slightly with roll angle, and with the attitude angle normal to the image plane (referred to here as the out of plane angle). Therefore, pattern-recognition image processing techniques could potentially determine all three attitude angles from a single image. Software was developed to generate pattern-matching templates using the 3D computer-aided design (CAD) model of the ballistic-range model, originally used in the design and fabrication of the models. Pattern recognition through template matching involves calculating the cross correlation between a shadowgraph image and a set of templates of the model at different attitudes, and finding the template attitude that results in the strongest correlation. Figure 34 shows side and top views of the 3D CAD model, and the 2D projections of each used as pattern-matching templates, of the ADEPT model at the attitude of the model in the shadowgraphs shown in Fig. 32. Cross-correlation coefficient maps are shown in Fig. 35 for the cross correlation between the side-view shadowgraph in Fig. 32(a) and (Fig. 35(a)) a template image at 0^o attitude, and (Fig. 35(b)) the template image in Fig. 34(c) at $\theta = 18.3^o$, $\psi = 4.9^o$, $\phi = -7.9^o$. The location of the peak cross-correlation coefficient, C_{max}, identifies the location of the object in the shadowgraph image best matching the

template, and can be related to the center of gravity, CG, of the model through the CAD model used to generate the template. The magnitude of C_{max} increases as the attitude of the template approaches that of the model image. Figure 36 shows the result of the template-matching search for the images in Fig. 32. The outline of the template images (Figs. 34(c) and (d), respectively) are overlaid on the shadowgraph images, and the CG location is marked in white.

The automated search procedure for finding the strongest correlation begins by calculating the maximum cross correlation coefficient, C_{max}, of the image with a template at 0° attitude ($\theta = \psi = \phi = 0^o$). For the side-view (pitch-plane) image, the template is rotated $\Delta\theta$ degrees and a new C_{max} is calculated. If the new C_{max} is greater, then the template is rotated another $\Delta\theta$ degrees. If it is less, then the search direction is changed. This is repeated until a peak is found to within $\pm\Delta\theta$ degrees. Then the step size is reduced and the process repeated until a step-size limit is reached. Figure 37 shows the variation in C_{max} with the template pitch angle, θ, for the side-view image in Fig. 32(a). Also shown are template images at the maximum C_{max} ($\theta = 18.3^o$) and one to either side of the peak. Figure 38 shows the impact of the out of plane template angle (the yaw angle, ψ, in this case) on C_{max}. Mismatches in the out of plane angle reduce the magnitude of C_{max}, but only a small effect on the location of the peak. In practice, both angles are searched iteratively. This figure also shows the potential for finding both in-plane and out-of-plane angles from a single image. This is more clearly illustrated in Fig. 39, which shows C_{max} as a function of template pitch angle, θ, for cross correlations with the top-view (yaw-plane) image of Fig. 32(b). There are two peaks, one corresponding to the pitch angle found in the side-view image ($\theta = 18.3^o$), and the other to a template at the negative of that angle. Due to the faceted shape of the ADEPT model, the templates for these two angles are slightly different, allowing the out-of-plane angle to be determined. In practice, only the in-plane angle is used for each shadowgraph, but the potential is there to recover both angles in the event that only one image of the orthogonal pair is obtained.

The faceted shape of the ADEPT model also makes possible finding the roll angle by this template-matching method. Figure 40 shows C_{max} as a function of template roll angle for both shadowgraphs in Fig. 32. In both cases the pitch and yaw angles of the templates were fixed at their respective optimal-match values ($\theta = 18.3^o$, $\psi = 4.9^o$). It is clear from the magnitude of C_{max} (compare Figs. 37-39) that template roll has a much weaker effect than pitch (or yaw - not shown). Also clear is the 45° circumferential symmetry of the heatshield facets. The data are smoother, and the effect of the model symmetry is more regular, in the top-view (yaw-plane) image in this example because at the high pitch angle and low yaw angle more of the heatshield surface is projected into the yaw-plane image than the pitch-plane image. It can also be seen in Fig. 40 that a slightly different value of the roll angle was found for the two shadowgraph views, in this case. As a result, manual assessment of the roll-angle match is required.

A set of test data were generated in order to evaluate the accuracy of template-matching film reading. One hundred sixty orthogonal pairs (320 images) of artificial "shadowgraph" images were generated for this purpose. An example pair is show in Fig. 41. All images were 3600 x 3600 pixels, representative of typical image sizes obtained with the Nikon D3200 cameras discussed above. The fiducial wire spacings and model sizes were based on HFFAF window diameters, with half using the 30 cm window diameter, and half the 38 cm diameter, giving image resolutions of 120 pixels/cm and 100 pixels/cm, respectively. The position and attitude of the model in each image pair were selected from uniformly distributed random numbers on the following intervals: $0 \le x, z \le 12.7$ cm, $-12.7 \le y \le 0$ cm (regions outlined by red boxes in Fig. 41), $-30^o \le \theta \le 30^o$, $-15^o \le \psi \le 15^o$, $-20^o \le \phi \le 20^o$.

A second set of images were generated from these to be more representative of real images. Gaussian noise was added and the images were then smoothed with a median filter to soften the model and wire edges. A random rotation between -2° and +2° was also applied to each image pair to represent the fact that rows and columns of the camera sensor arrays are not precisely aligned with the HFFAF test-section axes. The example images in Fig. 41 are rotated counter clockwise by 1.019°. Finally, the test images were distorted in a manner observed in real HFFAF images, which results in straight lines appearing curved. These distortions are due to misalignments between the image plane and optical axis, and imperfections in the optics, and existed prior to conversion to digital image recording. Unlike commonly-seen barrel and pincushion distortions, the direction and magnitude of curvature in the HFFAF images is uniform in each direction, as illustrated in Fig. 42. The film reading software assumes there are no distortions, and represents the fiducial wires as the linear least-squares fit to pixels identified as belonging to a given wire. Over the length of the shadowgraph station window, the deviations between the curved images of the wires and the linear fit are between 3 and 7 pixels for the plumb wires, less than 4 pixels for the catenary wires, and less than 2 pixels for the taut wires (top-view images). To

model this, a two-dimensional 2nd-order distortion was applied to each test image. The degree of distortion was defined by the maximum shift in the wire image in each direction, and was randomly selected from a uniform distribution between 0 and 12 pixels.

The test image sets were analyzed and the position and attitude residuals, i.e., the difference between the measured values and the actual values used to generate the images, are shown in Fig. 43 as histograms. The position residuals are given in terms of pixels, and the results are expected to be no better than ±1 pixel, since the model was positioned in the generated images to pixel resolution. It can be seen in Fig. 43 that the measured position residuals for the undistorted images are within ±1 pixel for nearly all cases, and that the spread is larger (~±2.5 pixels spanning three standard deviations (3σ) from the mean) for the distorted images. In terms of physical units, this corresponds to ~±0.3 mm in the distorted images. The difference in sign between the y and z mean residuals is due to the fact that the y origin fiducial wire lies near the top of the images, and the z origin fiducial wire lies near the bottom of the images, as indicated in Fig. 32.

The pitch and yaw angle 3σ residuals are ~±0.6°, however, likelihood of an exact match is higher for the undistorted images, as seen in Fig. 43(d) and (e). The uncertainty on roll angle determination is larger due to the issues discussed above (refer to Fig. 40). The actual roll angle was found in more cases for the undistorted images than for the distorted images, as seen if Fig. 43(f), however, the spread in residual was much larger for reasons still to be determined. As mentioned above, some user evaluation is required to verify the measured roll angle.

The position residuals are driven primarily by the image distortion. To illustrate this, the x residuals are plotted in Fig. 44(a) as a function of degree of horizontal image distortion, which equates to the degree of curvature of the plumb wire images. It can be seen in the figure that the residual, and scatter, increase with increasing image distortion. Figure 44(b) shows the x residuals as a function of vertical (z) position of the model. Here there is a general quadratic trend with z for the distorted images (not seen for the undistorted images), corresponding with the distorted shape of vertical lines, such as the plumb wires as sketched in Fig. 42. Digitally correcting known image distortions is currently under consideration as a future improvement to film-reading accuracy.

SUMMARY AND CONCLUSIONS

The NASA Ames HFFAF (Hypervelocity Free Flight Aerodynamics Facility) ballistic range was described. The various embodiments of the shadowgraph stations, including the optical element set-ups, were presented. This included the original stations with sheet film and configurations with two different types of digital cameras - Princeton Instruments/Acton PI-MAX2 cameras and Nikon D3200 cameras. The results of resolution tests for the 3 shadowgraph station configurations were presented and it was concluded that the PI-MAX2 cameras had less resolution than the film, but that the D3200 camera has nearly the same resolution as the film. The advantages of the digital cameras were discussed. The first and foremost advantage is the immediate availability of the shadowgraphs with the digital cameras, as opposed to a wait of 2 – 3 hours for film processing with the sheet film shadowgraph stations. An additional 2 – 3 hours is necessary to digitize the photos when sheet film is used. The images from the digital cameras are automatically digitized when the photos are taken.

The current shadowgraph station configuration is 26 stations with Nikon cameras with 6 selected vertical stations with PI-MAX2 cameras. Two types of trigger light sheet stations were described. One used visible light and the other, IR radiation. Three of the newer IR stations were installed, but it was concluded that the IR stations were more subject to spurious triggers than the visible light stations, so no more IR stations were installed.

The two gunpowders used for the NASA Ames 6.25”/1.50” light gas guns were presented. These were the Hercules HC-33-FS powder (no longer available) and the St. Marks Powder WC 886 powder. Data for the powders was presented. The results from eight proof shots over a muzzle velocity range of 3 to 5 km/s for the two powders were presented. Both muzzle velocities and piston velocities were 5 – 9% lower for the WC 886 powder than for the HC-33-FS powder. The muzzle velocity curves for the two powders were very nearly parallel, as were the two piston velocity curves. The experimental data and the results of CFD calculations for the piston velocities and muzzle velocities were in good agreement. The two rifles used to check out the shadowgraph stations were described. A rifle change was necessary on account of increasing difficulties in obtaining ammunition for the rifle originally used.

A shadowgraph-reading software that employs template-matching pattern recognition to locate the ballistic-range model was described. Templates are generated from the 3D CAD model of the ballistic-range

model. The accuracy of the approach was assessed using a set of computer-generated test images. The center of gravity of the model was located to within ±2.5 pixels (±0.3 mm) for images with distortions representative of typical shadowgraph images. Pitch and yaw angles were found to within ±0.6°. For the special case of a model with a faceted axial symmetry, it was possible to determine roll angle. Roll angle was determined to within ±1.8°, however, user evaluation was required to verify the measured roll angles.

ACKNOWLEDGEMENTS

Acknowledgements are due for the excellent work of the following team members: The gun crew was Donald B. Bowling and Adam K. Parish. Photography was by Jon-Pierre Wiens. Support by NASA (Contract NNA15BB15C) to Analytical Mechanics Associates, Inc. is gratefully acknowledged.

REFERENCES

1. Wilder, M. C., Bogdanoff, D. W., and Cornelison, C. J., "Hypersonic Testing Capabilities at the NASA Ames Ballistic Ranges," AIAA 2015-1339, 53rd AIAA Aerospace Sciences Meeting, January 2015.
2. Cornelison, C. J., "Status Report for the Hypervelocity Free-Flight Aerodynamic Facility," 48th Aeroballistic Range Association Meeting, November 1997.
3. Wilder, M. C., Reda, D. C., and Prabhu, D. K., "Heat-Transfer Measurements on Hemispheres in Hypersonic Flight through Air and CO_2," AIAA-2011-3476, 42nd AIAA Thermophysics Conference, 27 - 30 June 2011.
4. Bogdanoff, D. W., Brown, J. D., Dyakonov, A. A., and Wilder, M. C., "New Developments in Diagnostic, Launch and Model Control Techniques in the NASA Ames Ballistic Ranges," 63rd Meeting of the Aeroballistic Range Association, September-October, 2012.
5. Bogdanoff, D. W., and Wilder, M. C., "Sabot, Obturator and Gas-In-Launch Tube Techniques for Heat Flux Models in Ballistic Ranges," 64th Meeting of the Aeroballistic Range Association, October 6 - 11, 2013.
6. Wilder, M. C., Bogdanoff, D. W., and Saunders, D. A., "Heat Transfer Measurements on the Afterbody of Spheres in Hypersonic Free-Flight in Air and Carbon Dioxide," AIAA 2015-2966, 53rd AIAA Aerospace Sciences Meeting, 5-9 January 2015.
7. Brown, J. D., Bogdanoff, D. W., Yates, L. A., Wilder, M. C., and Murman, S. M., "Complex-Trajectory Aerodynamics Data for Code Validation from a New Free-Flight Facility," AIAA 2006-662, 44th AIAA Aerospace Sciences Meeting, 9 - 12 January 2006.
8. Canning, T. N., Seiff, A. and James, C. S., "Ballistic Range Technology," AGARDograph 138, published by the North Atlantic Treaty Organization, Advisory Group for Aerospace Research and Development (AGARD), August, 1970, p. 241.
9. ibid., p. 245.
10. Bogdanoff, D. W., "New Higher-Order Godunov Code for Modelling Performance of Two-Stage Light Gas Guns," NASA TM 110363, September, 1995.
11. Bogdanoff, D. W., "CFD Modelling of Bore Erosion in Two-Stage Light Gas Guns, NASA TM-1998-112236, August, 1998.
12. Bogdanoff, D. W., personal communications with staff of St. Marks Powder, Inc. in Florida.
13. Riefler, D. W. and Lowery, D. J., "Linear Burn Rates of Ball Propellants Based on Closed Bomb Firings," Ballistic Research Laboratories (BRL) Contractor Report No. 172, August, 1974.
14. Yates, L. A., "A Comprehensive Automated Aerodynamic Reduction System for Ballistic Ranges," Wright Laboratory, Armament Directorate, WL-TR-95-7059, Oct. 1996.
15. Hergert, J. D., Brock, J. M., Stern, E. C., Wilder, M. C., and Bogdanoff, D. W., "Free-Flight Trajectory Simulation of the ADEPT Sounding Rocket Test Using CFD," AIAA 2017-4462, 35th AIAA Applied Aerodynamics Conference, 5-9 June 2017.
16. Space Technology Game Changing Development, "ADEPT SR-1 Flight Experiment," NASA Facts, FS-2017-03-01-ARC, https://gameon.nasa.gov/gcd/files/2017/03/ADEPT_SR-1_FS_170301.pdf

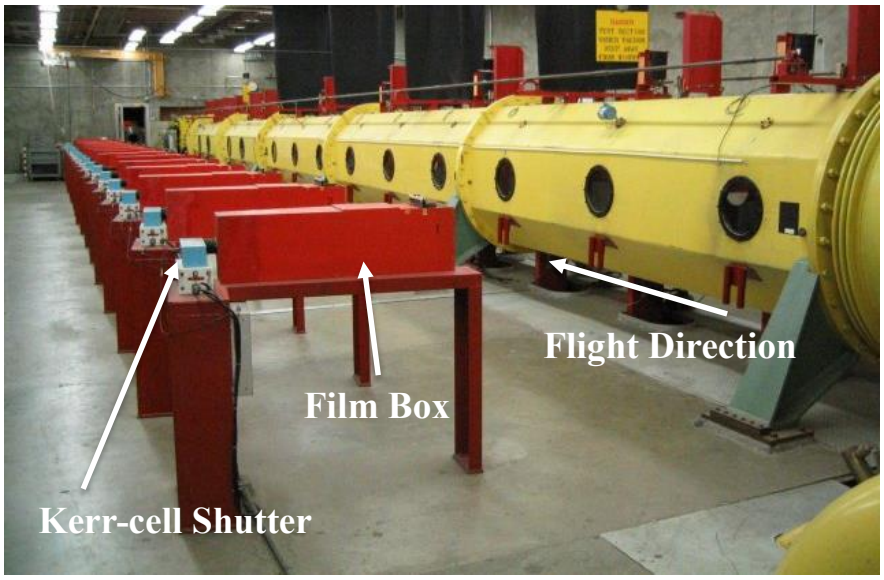

Fig. 1. HFFAF test section and original horizontal shadowgraph camera stations, looking west. Shadowgraph camera stations and Kerr cells will be discussed in the text.

Fig. 2. HFFAF test section and original horizontal shadowgraph camera stations, looking east.

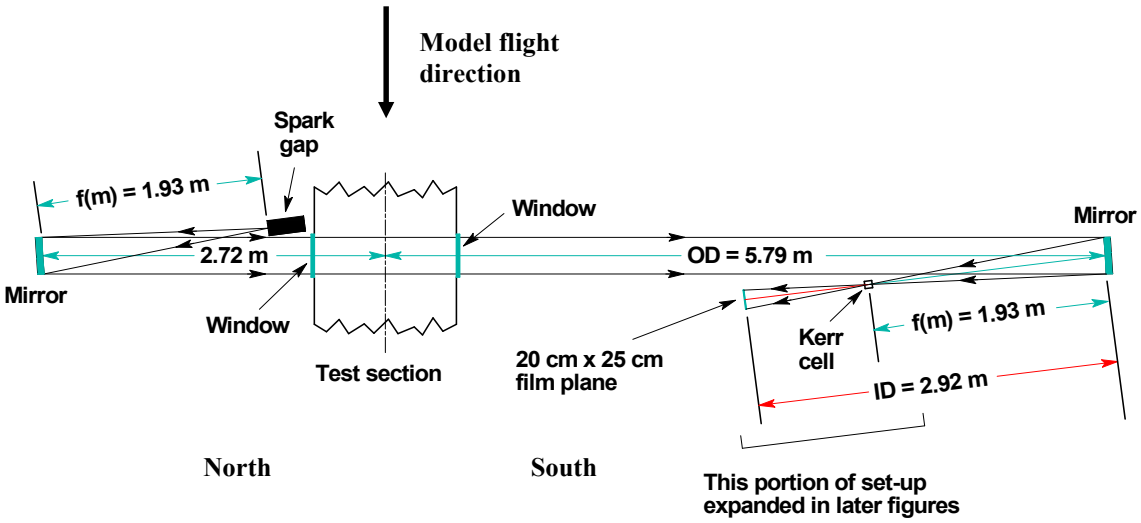

Fig. 3. Top view sketch of optical set-up for an original horizontal shadowgraph camera station. Top and bottom test section windows have been omitted for clarity.

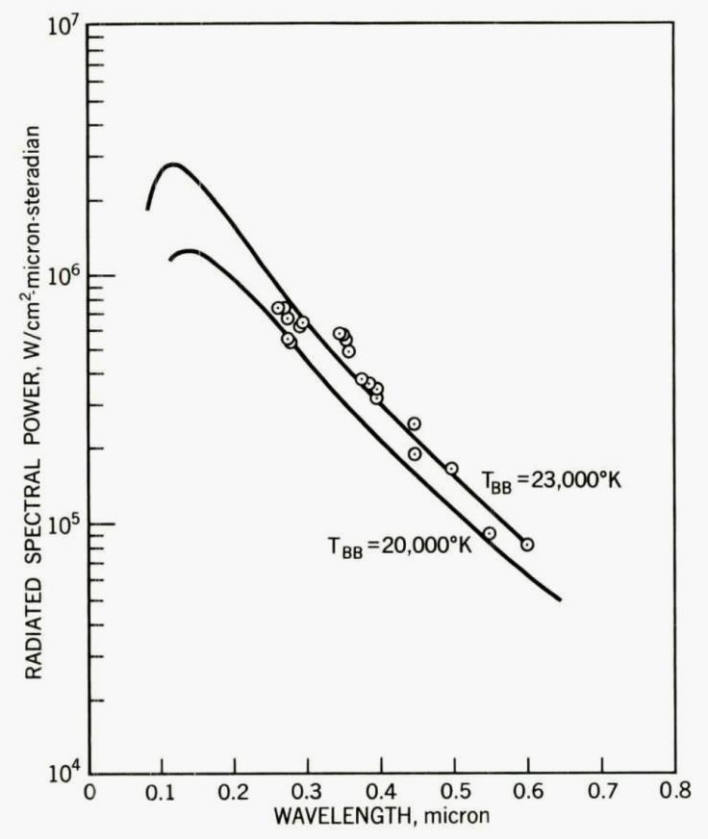

Fig. 4. Radiated power as a function of wavelength for the spark gap.

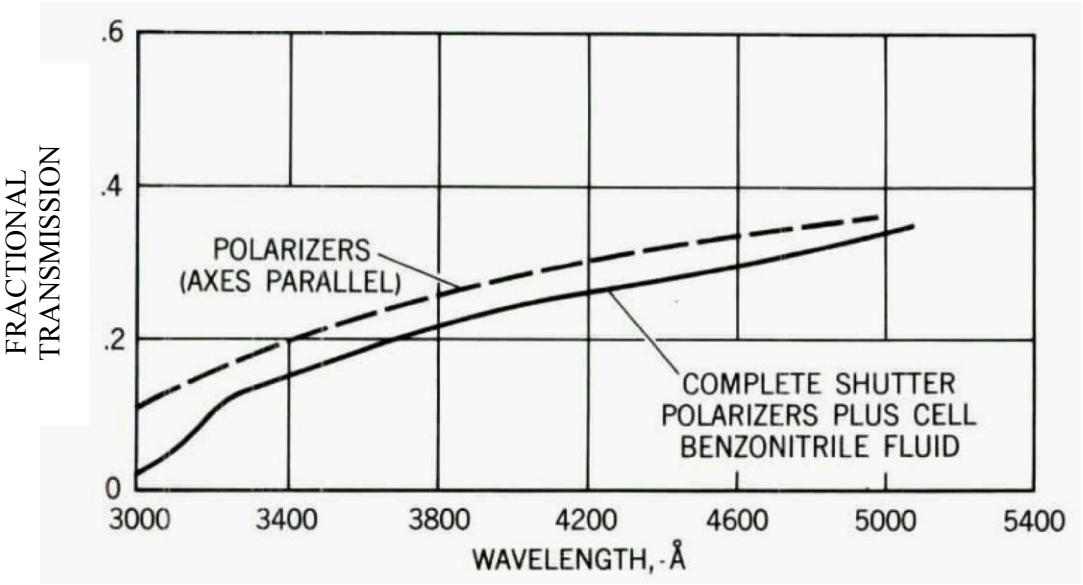

Fig. 5. Spectral transmissivity of parallel polarizers and complete Kerr cell.

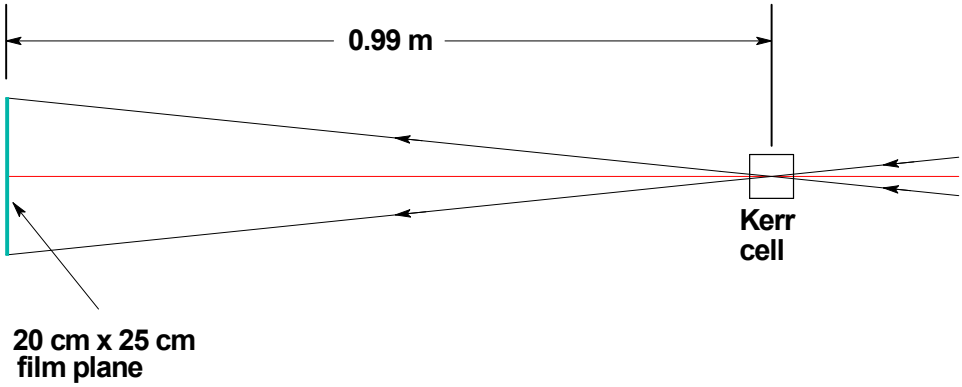

Fig. 6. Enlarged view of final section of optical path of Fig. 3, showing Kerr cell and film plane.

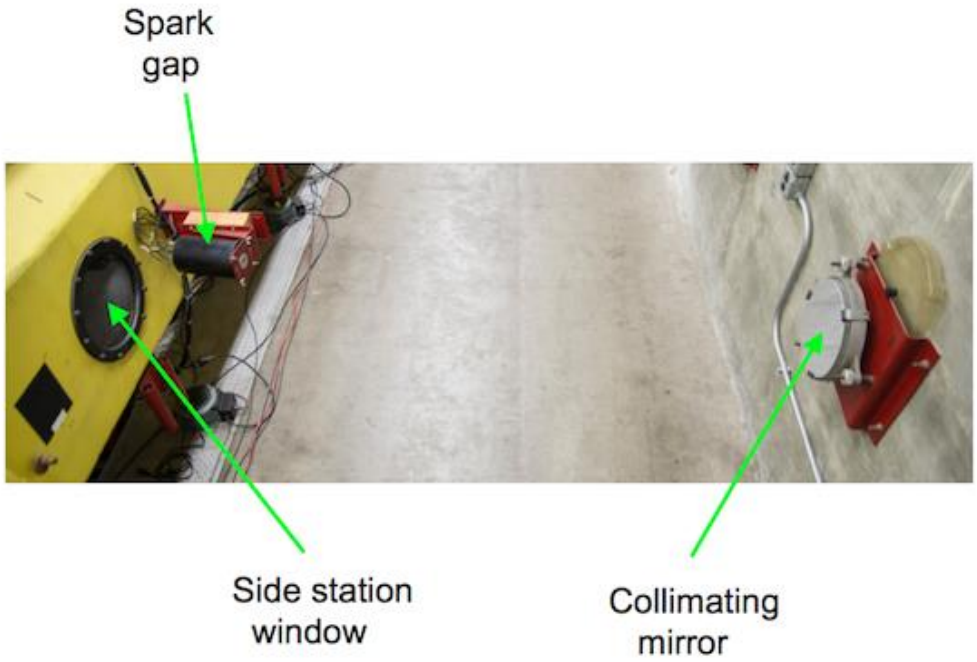

Fig. 7. Spark gap and collimating mirror on north side of test section.

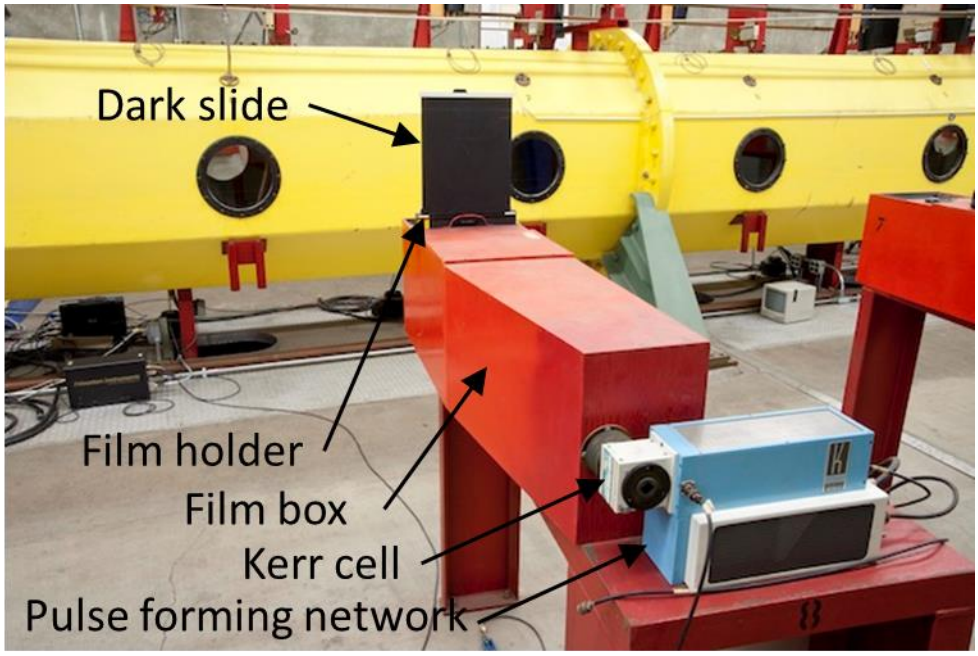

Fig. 8. HFFAF test section and an original horizontal shadowgraph camera station, single station, looking north. Film box is red, Kerr cell assembly is blue and white, in foreground.

Fig. 9. An original horizontal shadowgraph camera station, looking south. Red film box is in foreground, hiding the Kerr cell assembly. The focusing mirror is in the background.

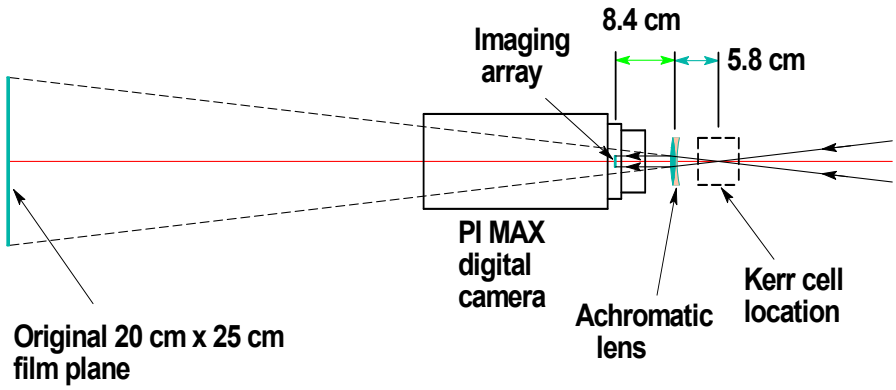

Fig. 10. Final section of optical path for a shadowgraph station with a PI-MAX camera. Corresponds to Fig. 6 for an original sheet film station. Note that Kerr cell is not used with ICCD camera.

Fig. 11. HFFAF test section and a PI-MAX shadowgraph camera station, looking northeast. The camera, imaging lens and Kerr cell assembly without the Kerr cell are visible.

Fig. 12. A PI-MAX shadowgraph camera station, looking south. The camera, imaging lens and Kerr cell assembly without the Kerr cell are visible in foreground. The focusing mirror is in the background.

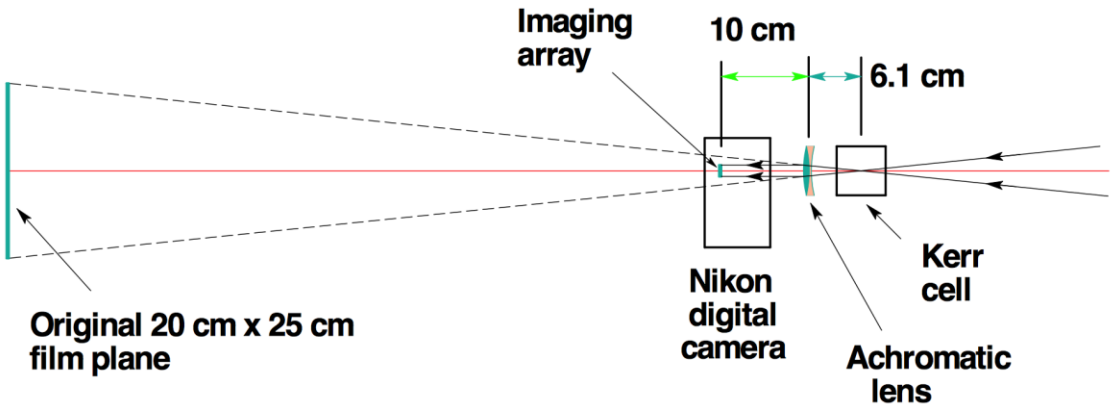

Fig. 13. Final section of optical path for a shadowgraph station with a Nikon camera. Corresponds to Fig. 6 for an original sheet film station.

Fig. 14. HFFAF test section and a Nikon shadowgraph camera station, looking northeast. The camera and Kerr cell assembly are visible. The imaging lensis just to the left of the Kerr cell.

Fig. 15. A Nikon shadowgraph camera station, looking south. The camera and the Kerr cell assembly are visible in the foreground. The imaging lens is sandwiched in between the Kerr cell and the camera. The focusing mirror is in the background.

Fig. 16. HFFAF test section and Nikon shadowgraph camera stations, looking west. This photo corresponds to Fig. 1, which shows the original horizontal sheet film shadowgraph stations.

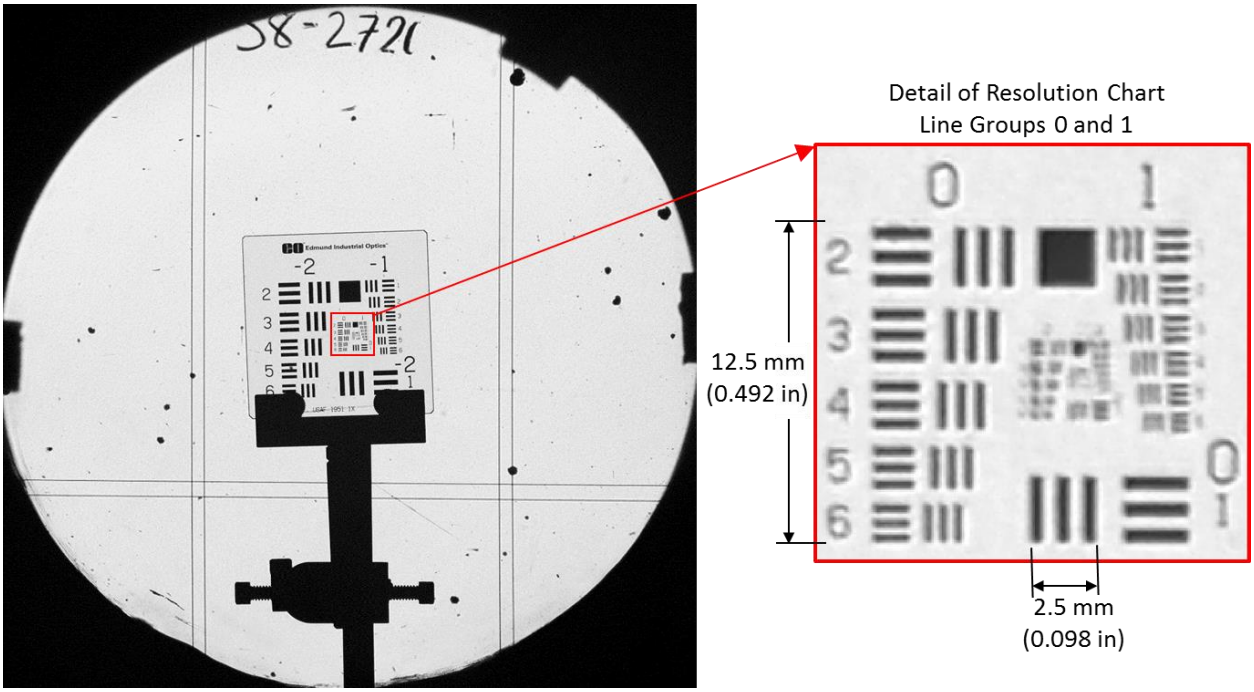

Fig. 17. Image of USAF 1951 resolution chart located at center of HFFAF test section at station 8 and detail of chart groups 0 and 1.

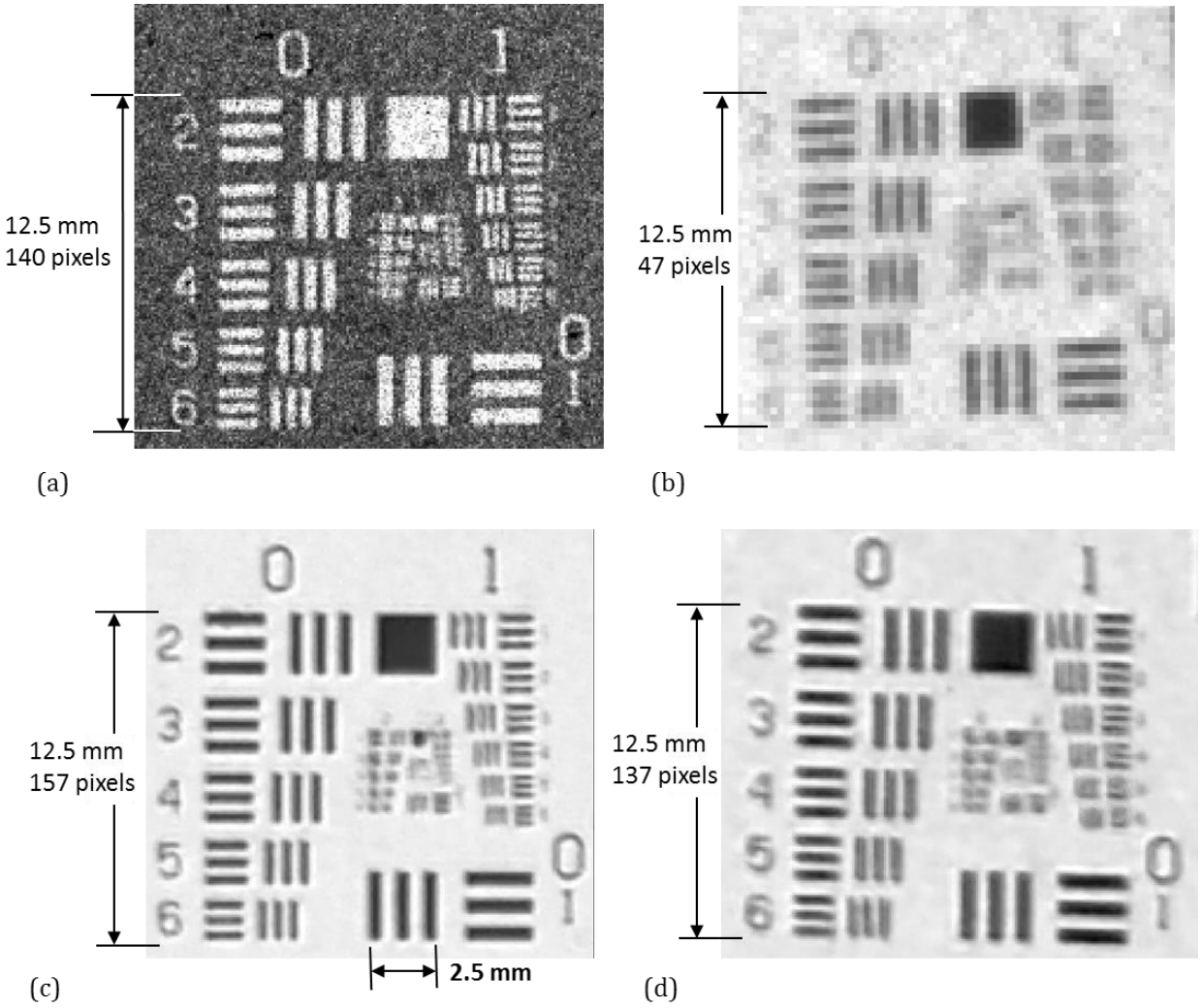

Fig. 18. Images of USAF 1951 resolution chart obtained with (a) original sheet film shadowgraph station, (b) with shadowgraph station using ICCD camera, (c) digital SLR camera at a station with 30 cm window, and (d) digital SLR camera at a station with 36 cm window.

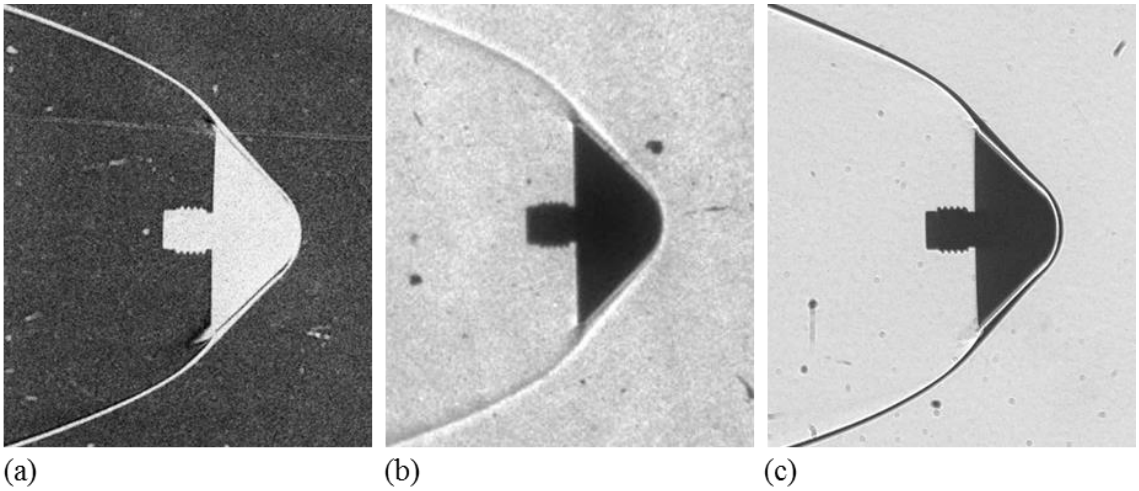

Fig. 19. Shadowgraph images of a 33 mm diameter, 45° half angle, blunt cone in flight at 2700 m/s: (a) digitized sheet film negative; (b) ICCD camera image; (c) digital SLR image.

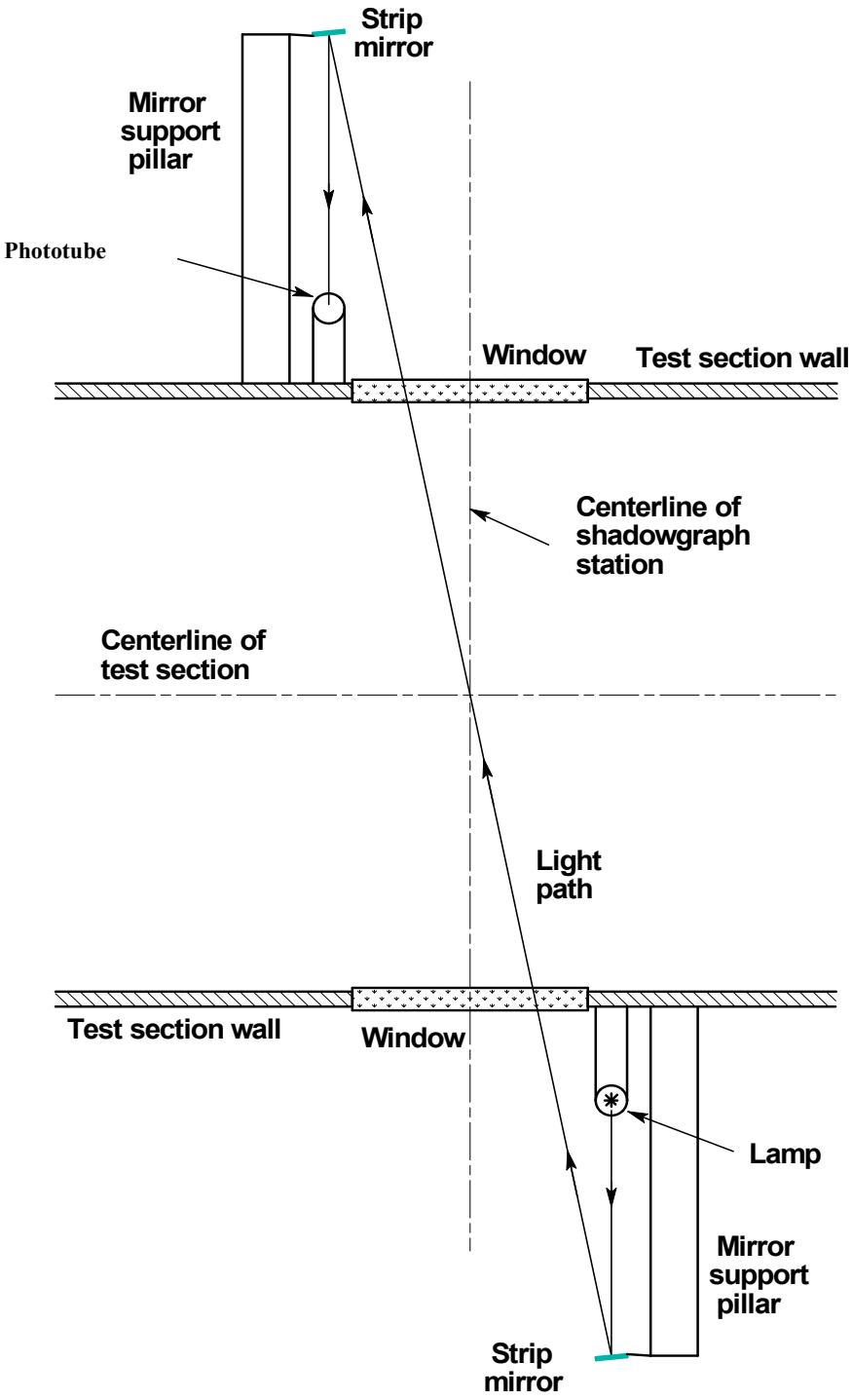

Fig. 20. Side view sketch of optical set-up for original visible light sheet trigger stations

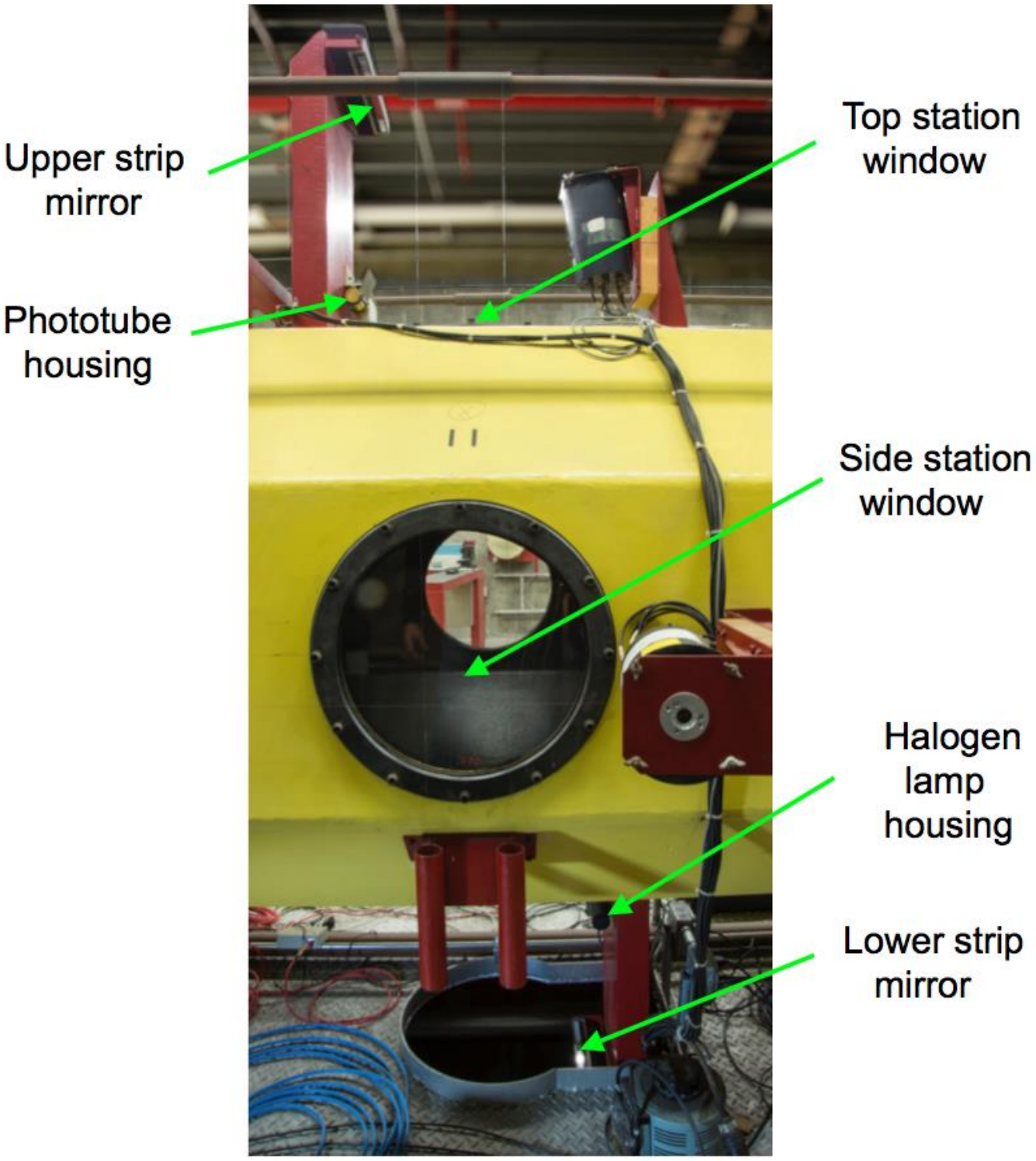

Fig. 21. Side view photograph of an original visible light sheet trigger station.

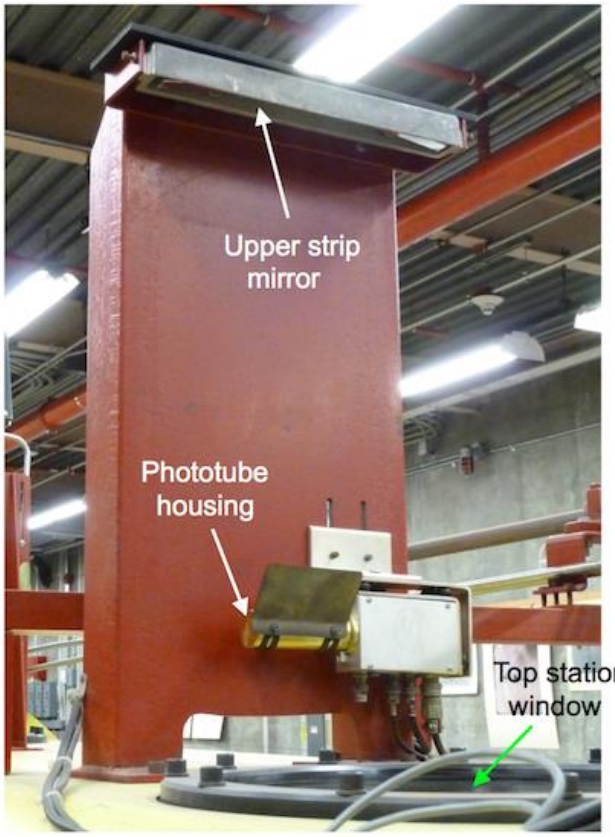

Fig. 22. Photograph of the upper components of an original visible light sheet trigger station.

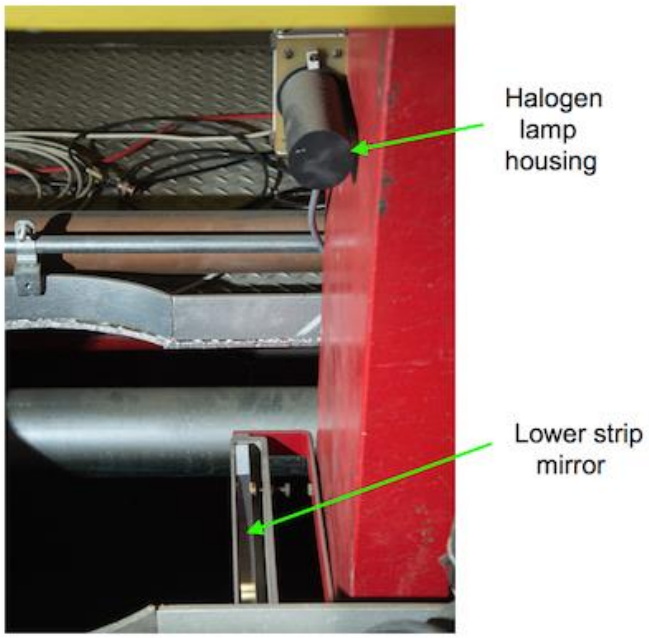

Fig. 23. Photograph of the lower strip mirror and lamp housing of an original visible light sheet trigger station.

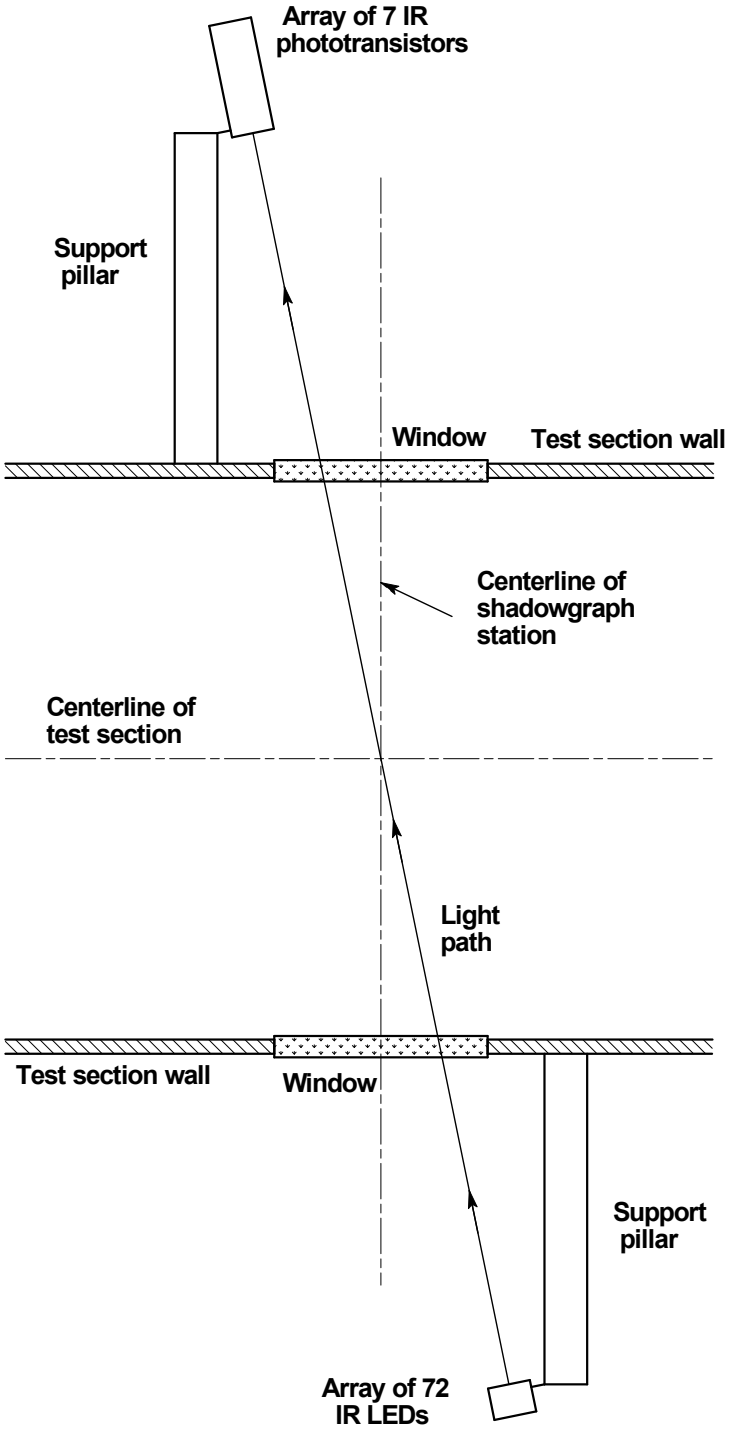

Fig. 24. Side view sketch of optical set-up for light sheet trigger stations with IR LEDs and IR phototransistors.

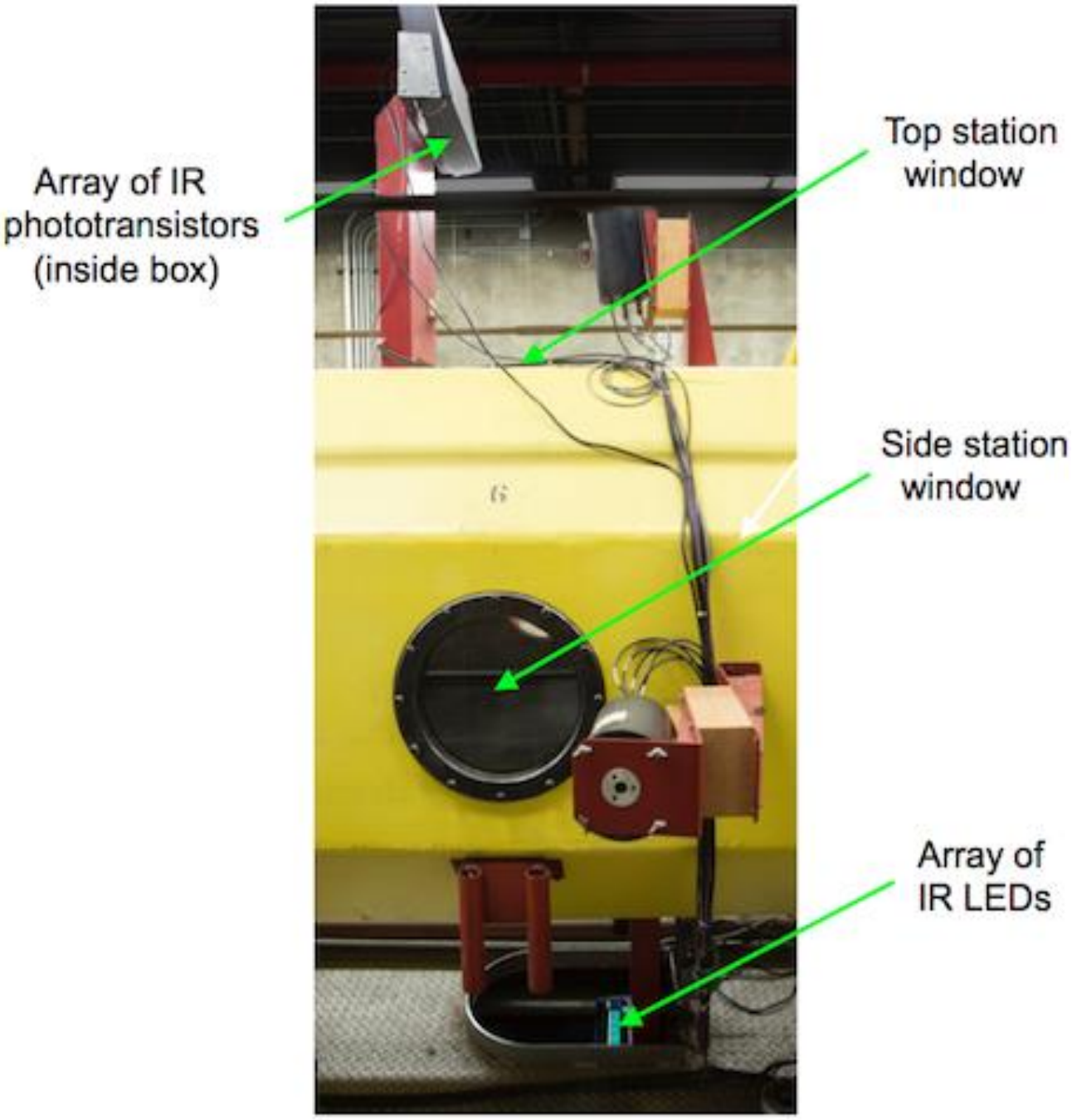

Fig. 25. Side view photograph of an IR light sheet trigger station.

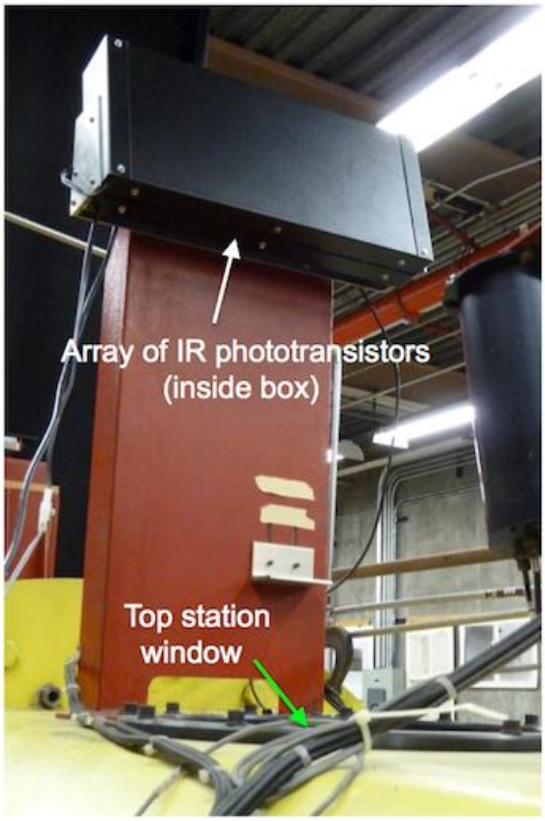

Fig. 26. Photograph of the upper components of an IR light sheet trigger station.

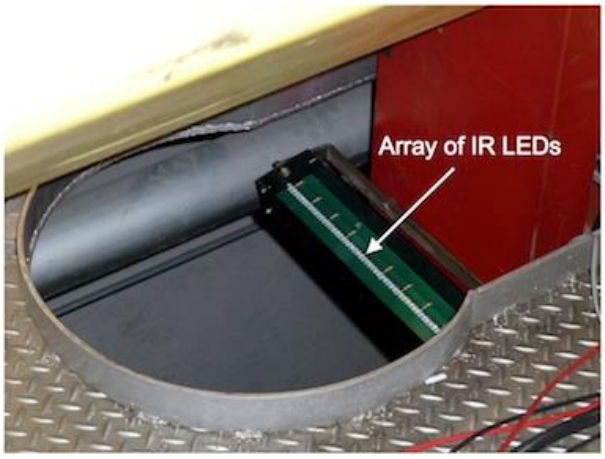

Fig. 27. Photograph of IR LED array of an IR light sheet trigger station.

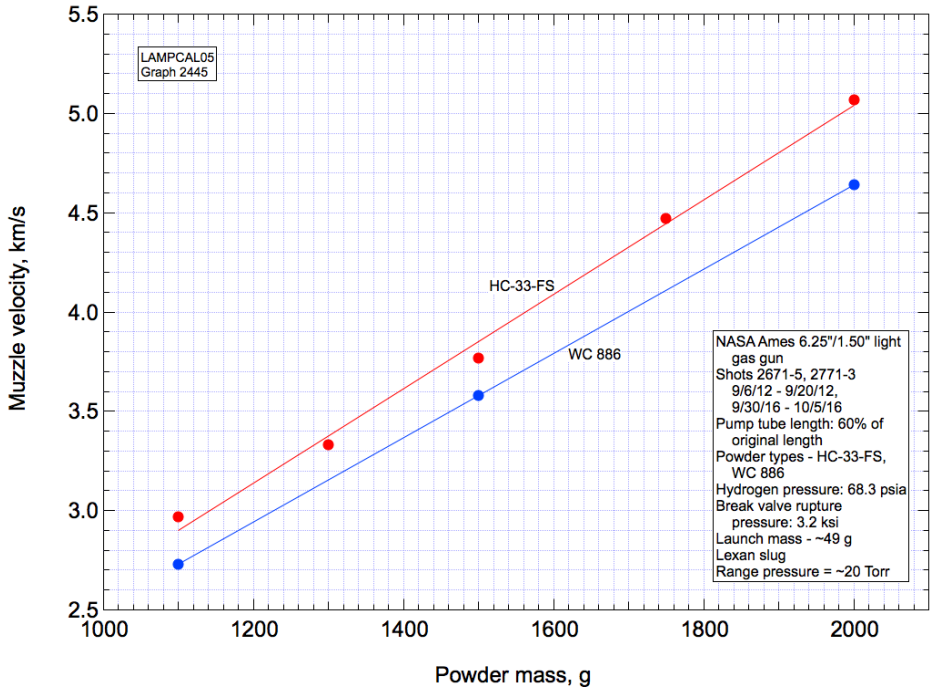

Fig. 28. Muzzle velocity versus powder mass for proof shots with HC-33-FS and WC 886 powders.

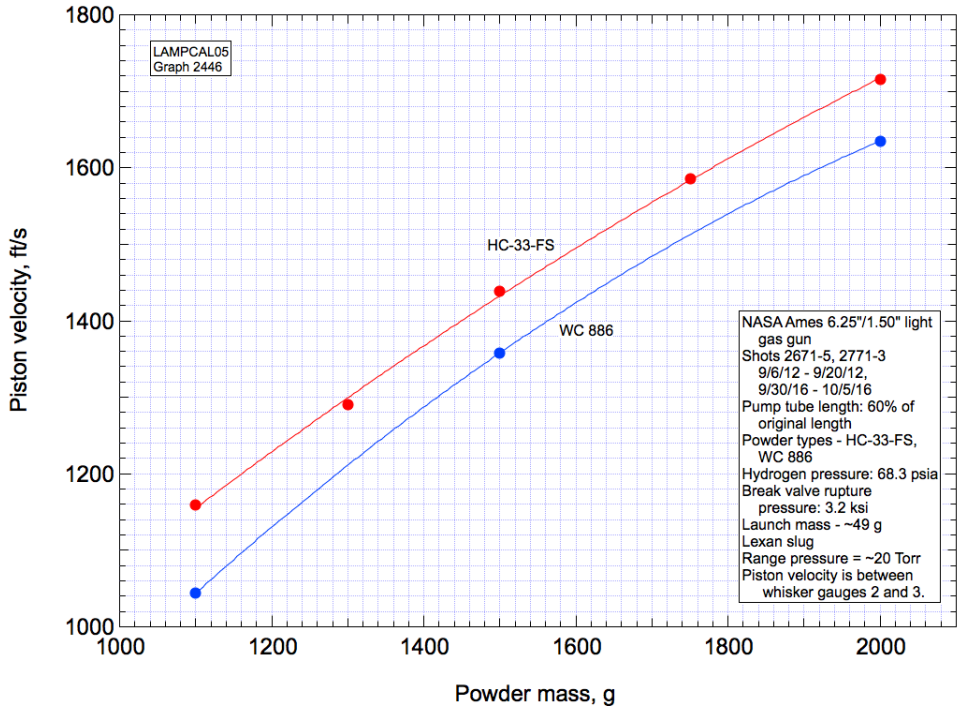

Fig. 29. Piston velocity versus powder mass for proof shots with HC-33-FS and WC 886 powders.

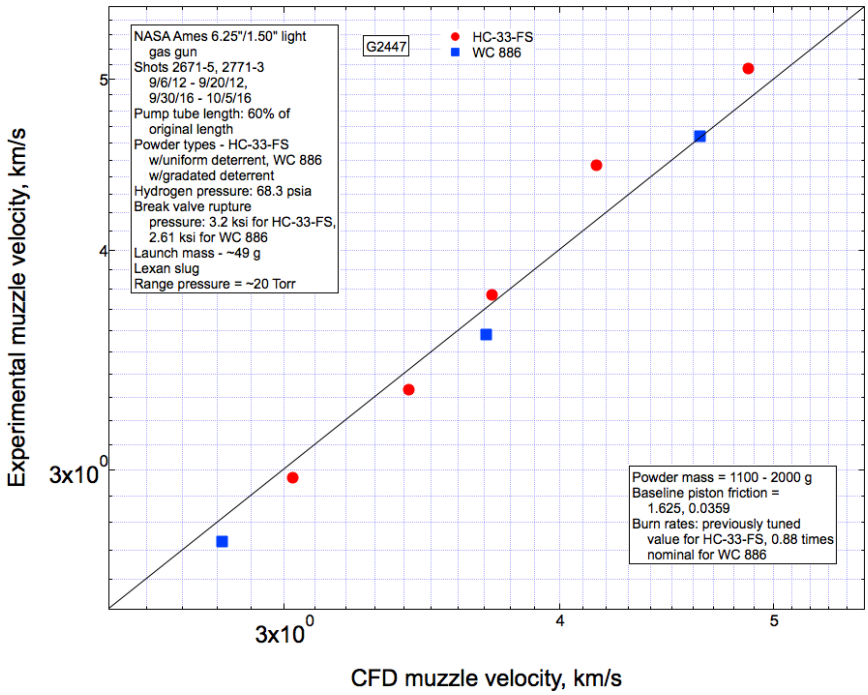

Fig. 30. Experimental versus CFD muzzle velocity for proof shots with HC-33-FS and WC 886 powders.

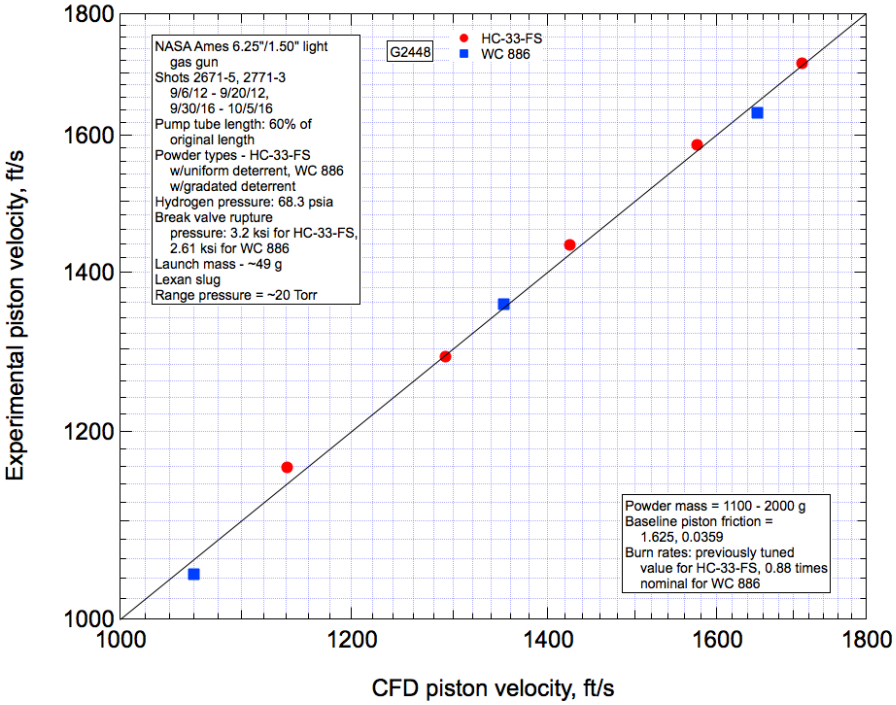

Fig. 31. Experimental versus CFD piston velocity for proof shots with HC-33-FS and WC 886 powders.

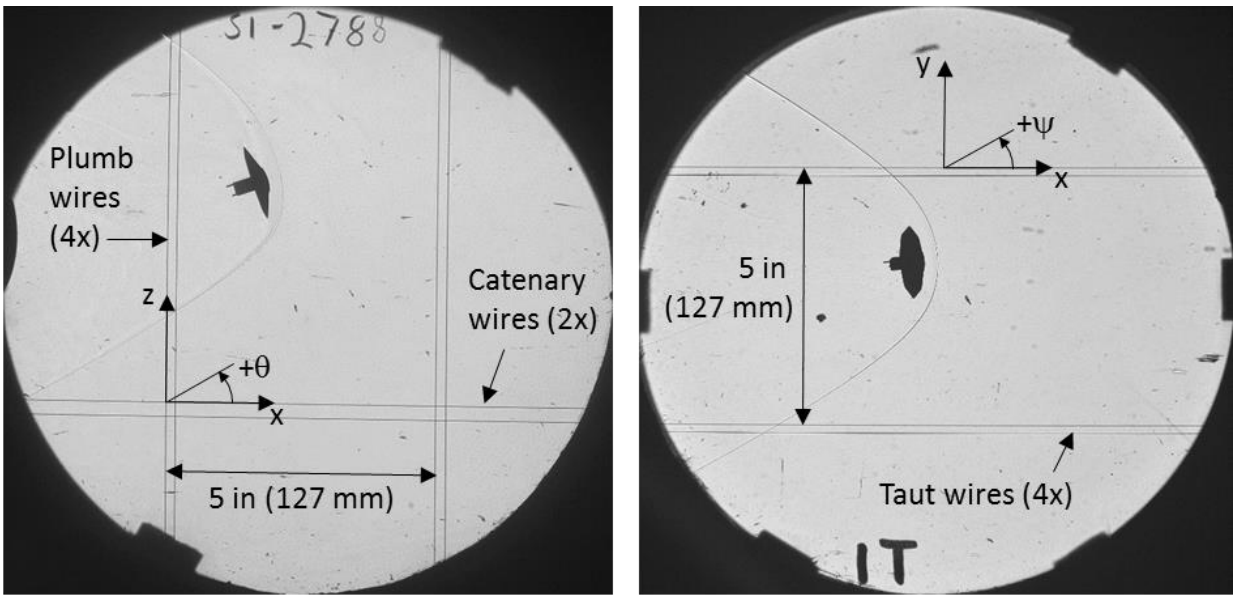

Fig. 32. Orthogonal pair of shadowgraphs images at HFFAF Station 1: (a) side view (pitch plane, θ); (b) top view (yaw plane, ψ).

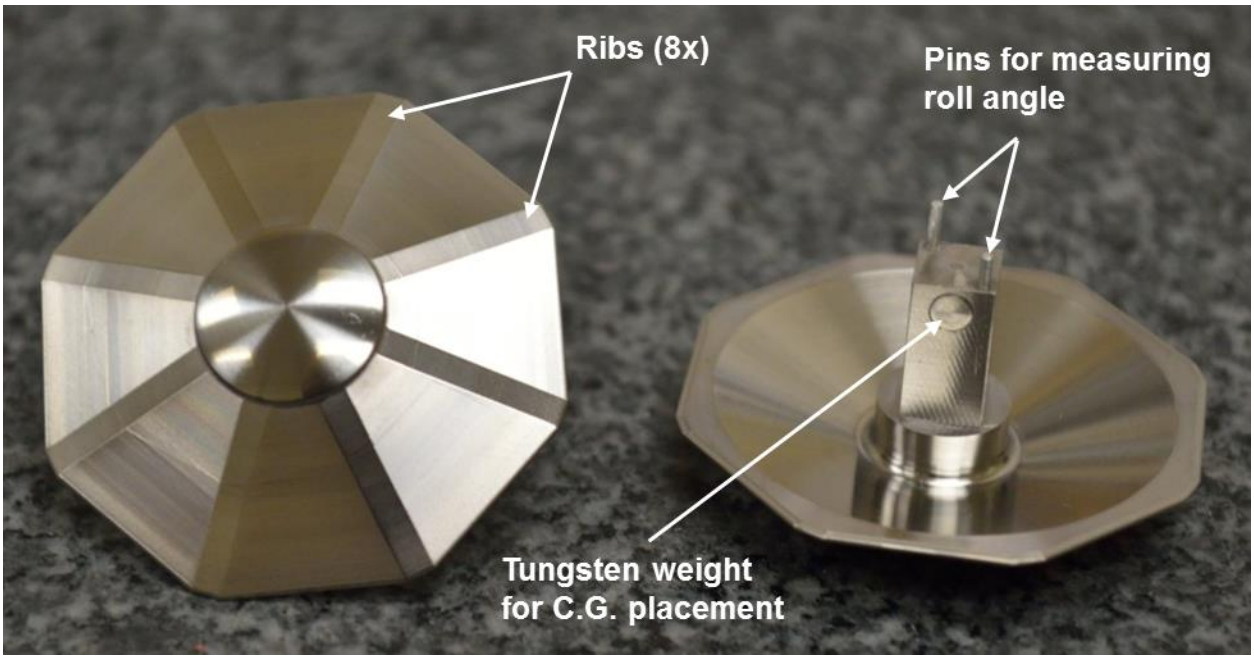

Fig. 33. ADEPT SR-1 ballistic range models, 3.56 cm diameter at rib tips.

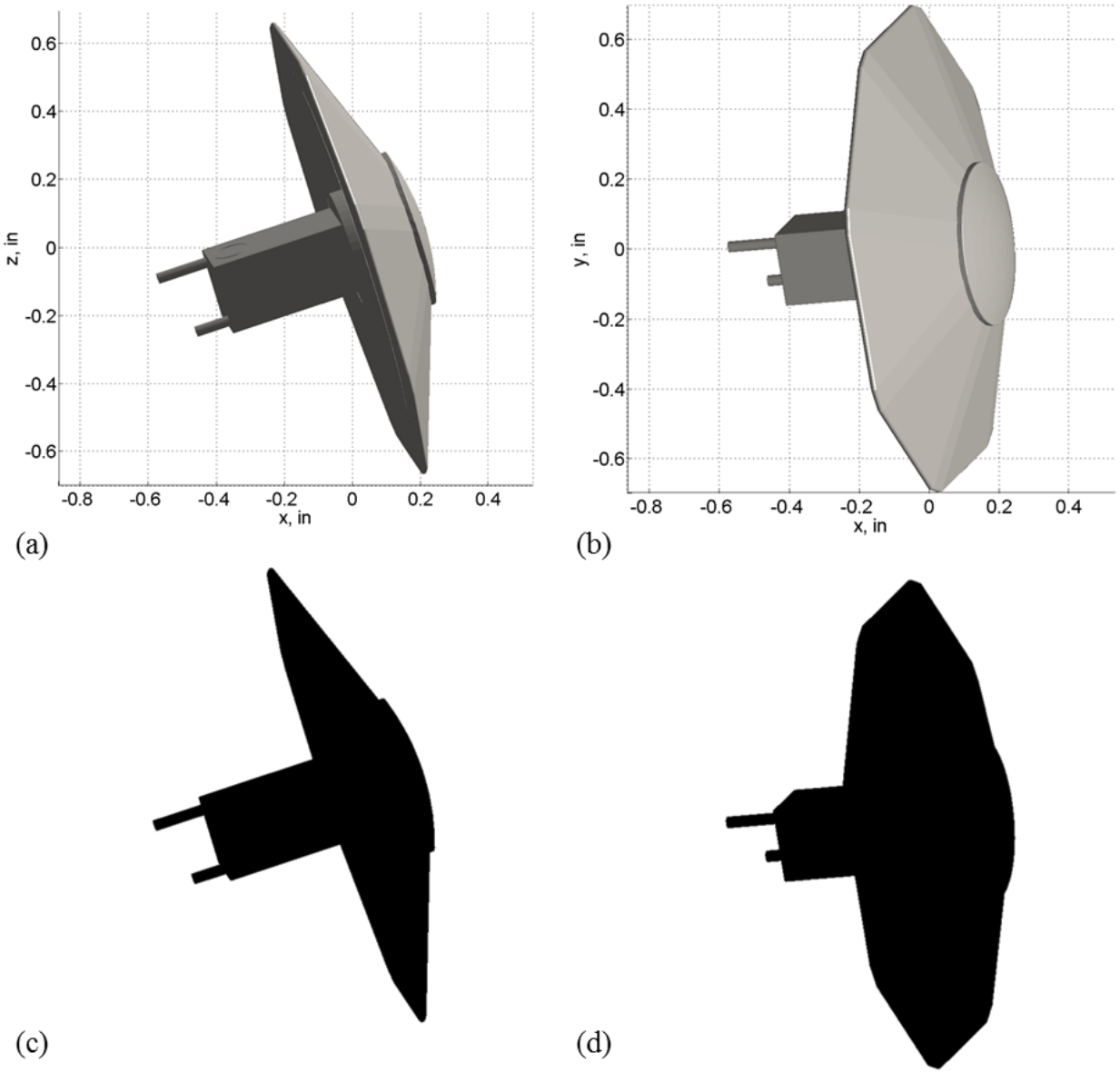

Fig. 34. ADEPT SR-1 at $\theta = 18.3^{o}$, $\psi = 4.9^{o}$, $\phi = -7.9^{o}$, Station 1, Shot 2788: (a) CAD model, side view; (b) CAD model, top view; (c) pattern-matching template, side view; (d) pattern-matching template, top view.

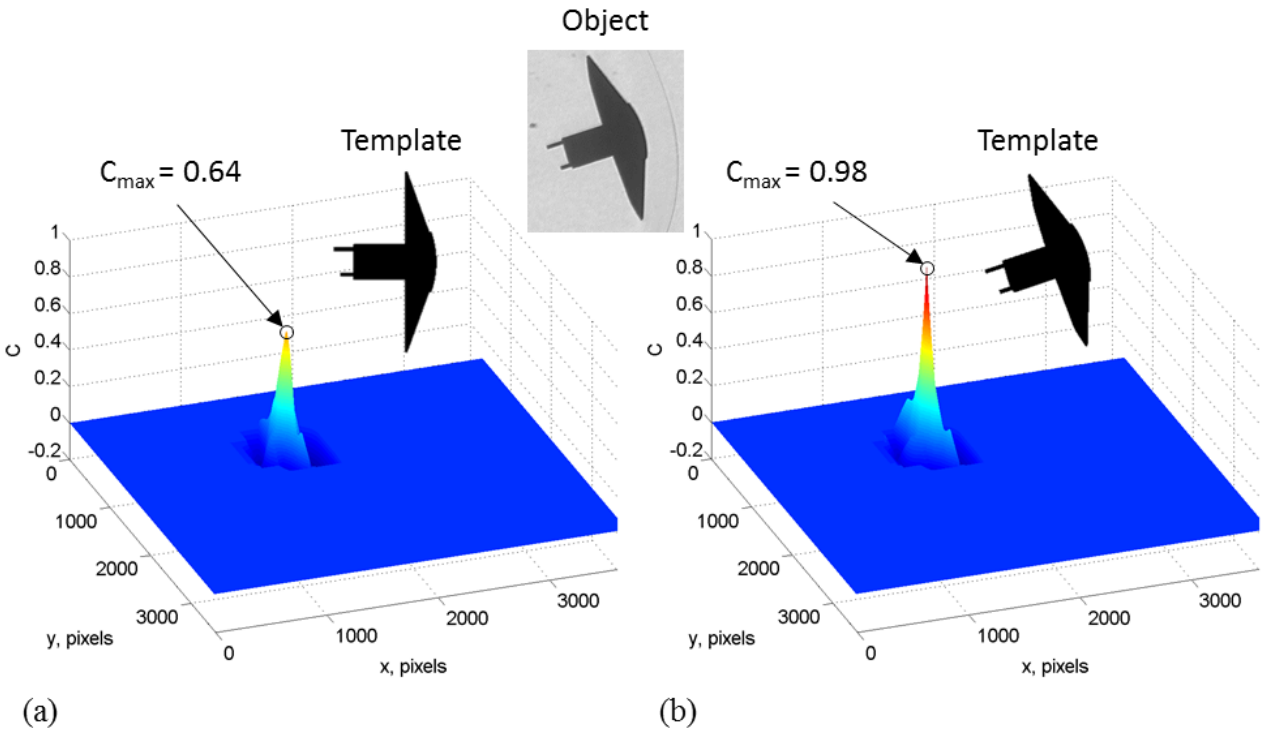

Fig. 35. Coefficient maps for cross correlation between shadowgraph image shown in Fig. 32(a) (target object inset, above) and template images at (a) $\theta = \psi = \phi = 0^o$, and (b) $\theta = 18.3^o$, $\psi = 4.9^o$, $\phi = -7.9^o$, (template shown in Fig. 34(c)).

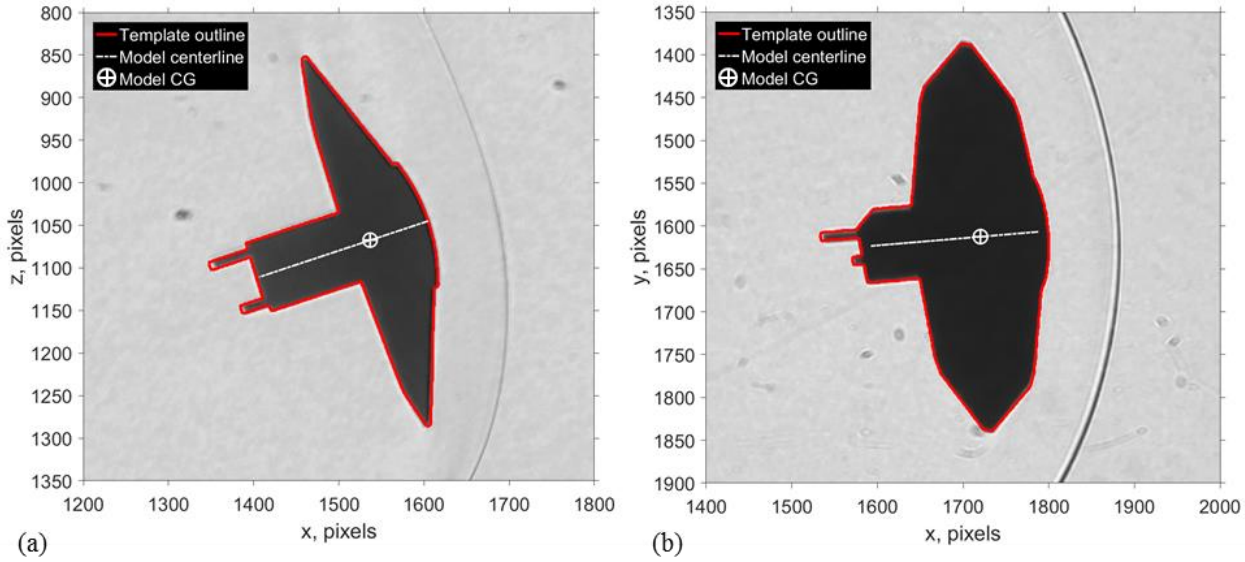

Fig. 36. Pattern-matching results for shadowgraphs in Fig. 32: (a) side view (pitch plane, θ) image; (b) top view (yaw plane, ψ) image.

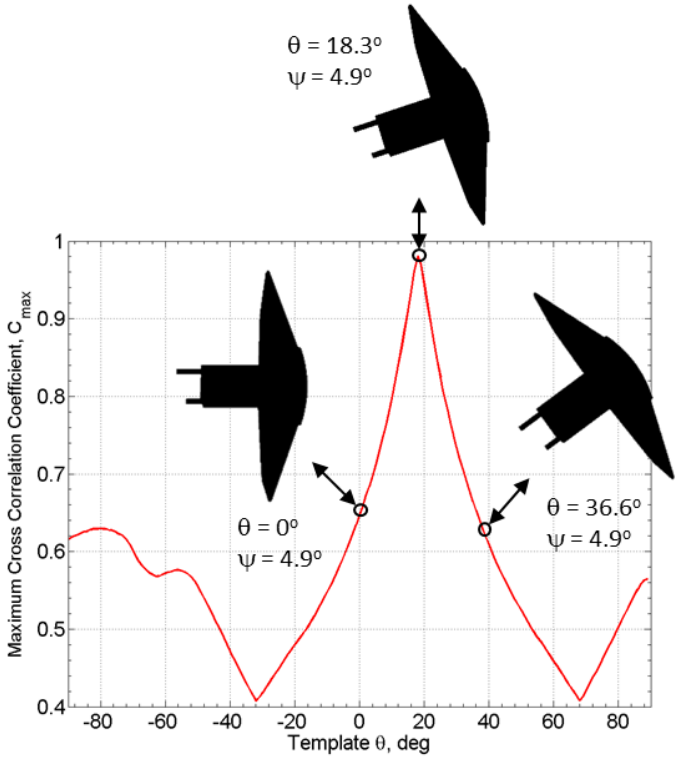

Fig. 37. Maximum cross correlation coefficient, C_{max}, as a function of template pitch angle, q, for shadowgraph image shown in Fig. 32(a). All templates were at $\psi = 4.9^{o}$ and $\phi = -7.9^{o}$.

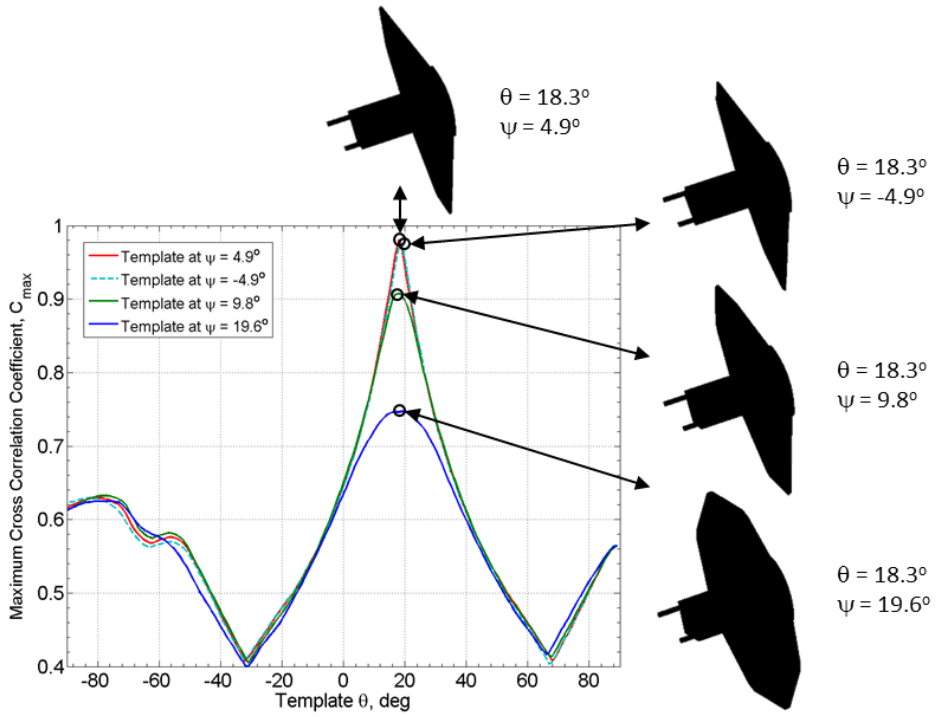

Fig. 38. Effect of out-of-plane template angle on in-plane angle template matching. Maximum cross correlation coefficient, C_{max}, as a function of template pitch angle, q, for shadowgraph image in Fig. 32(a). For each curve the template ψ was held at the indicated value. All templates were at the same ϕ.

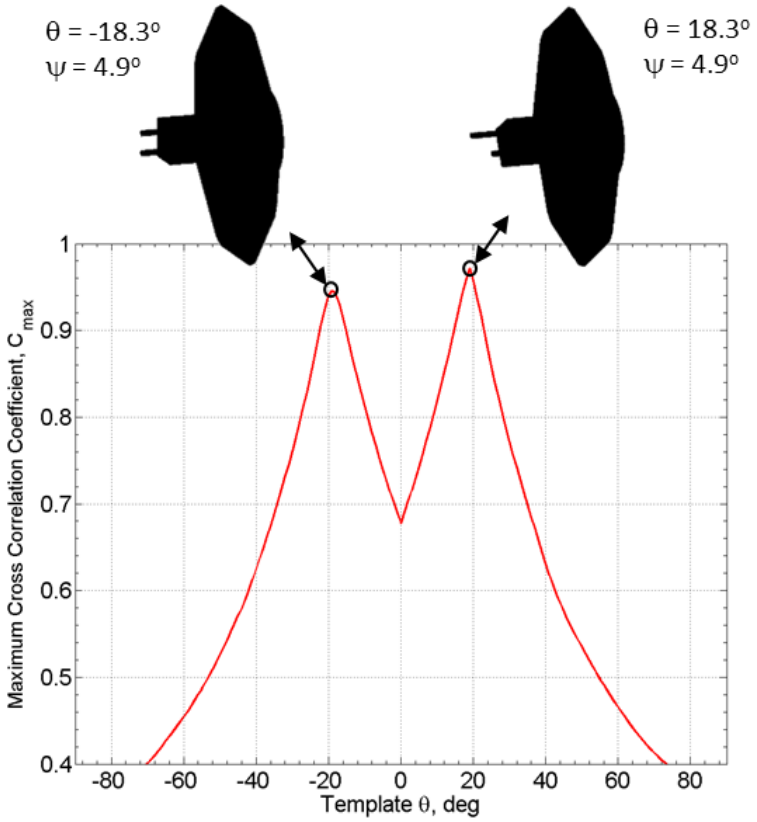

Fig. 39. Identifying out-of-plane angle: Curve shows maximum cross correlation coefficient, C_{max}, as a function of template pitch angle, q, for top view shadowgraph shown in Fig. 32(b). All templates at the same ψ and ϕ.

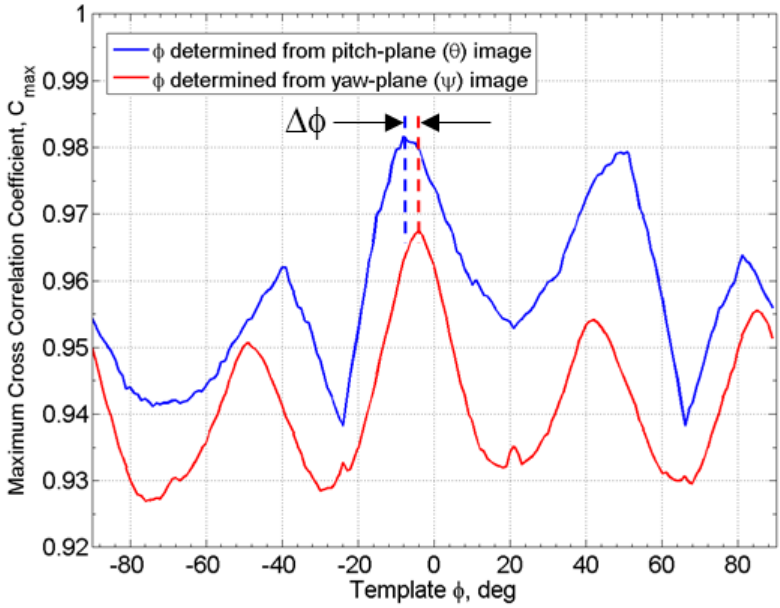

Fig. 40. Roll angle identification: Curves show maximum cross correlation coefficient, C_{max}, as a function of template roll angle, ϕ, for shadowgraphs shown in Fig. 32. All templates at the same q and ψ.

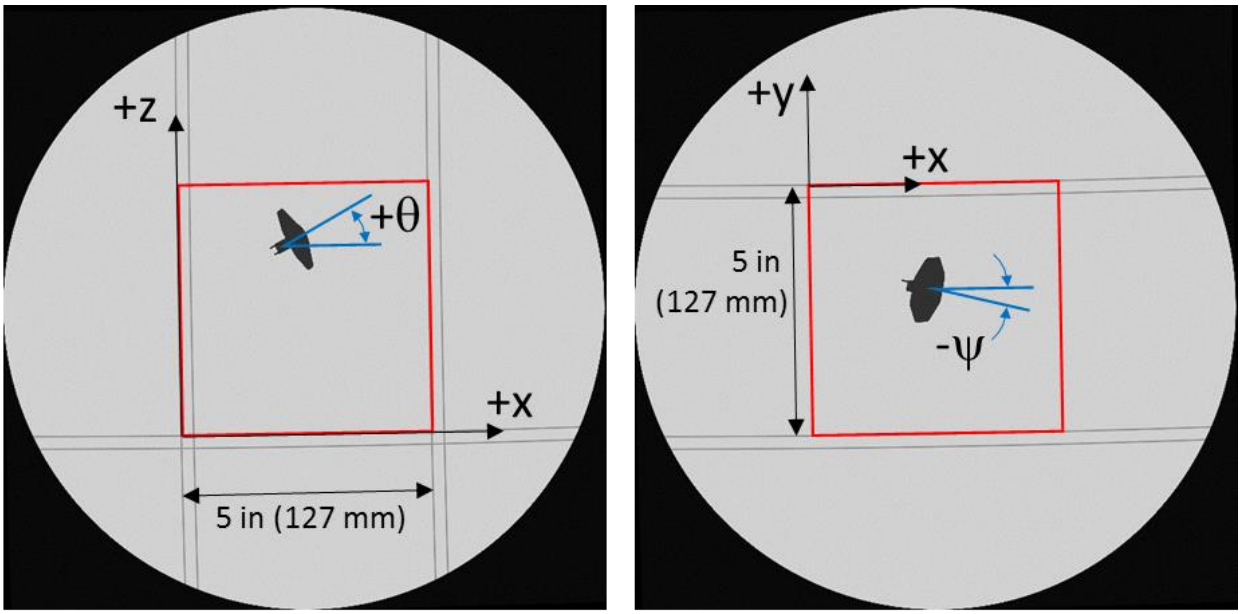

Fig. 41. Artificially-generated "shadowgraph" image pair used to evaluate pattern-matching accuracy, and coordinate system definition: (a) side view (pitch plane, θ); (b) top view (yaw plane, ψ). Model CG was randomly positioned within the region bounded by the red box.

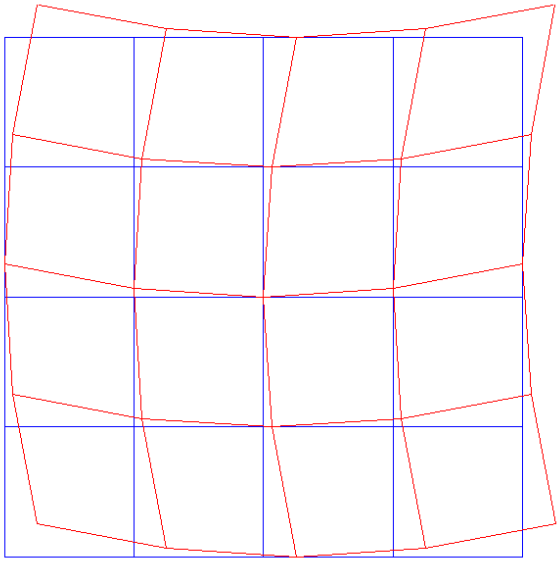

Fig. 42. Exaggerated illustration of typical image distortions.

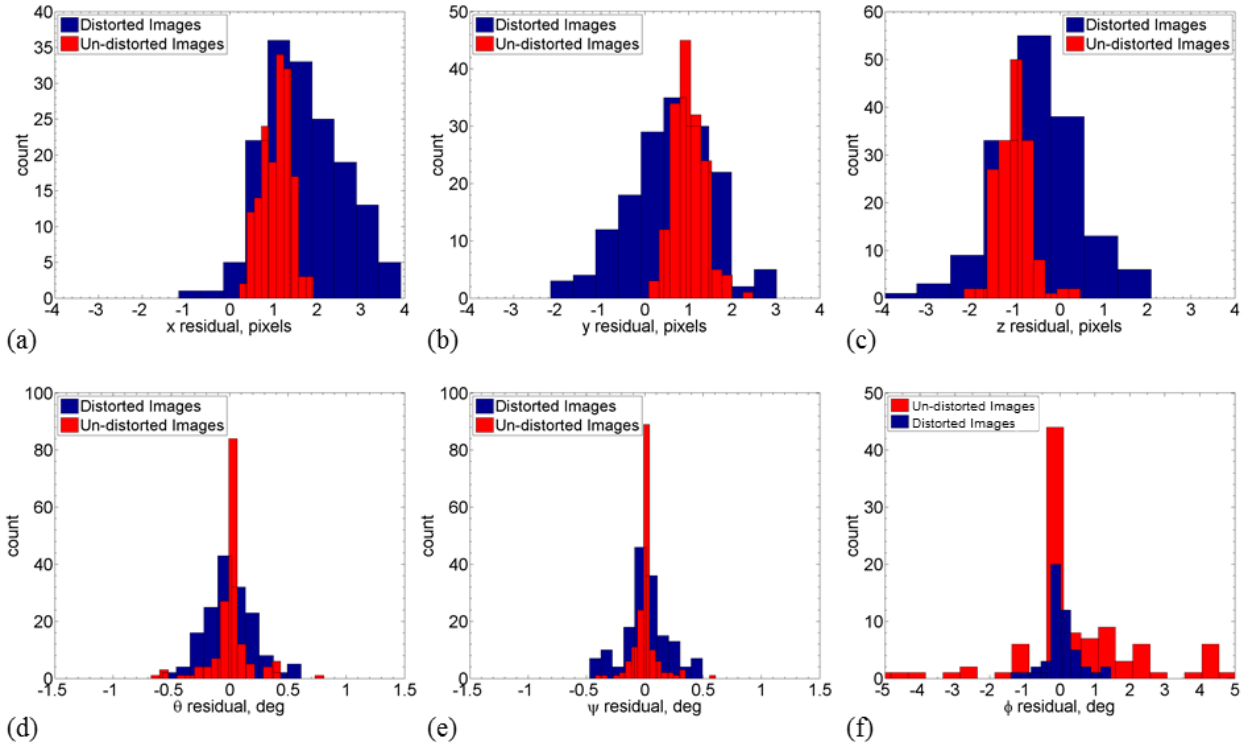

Fig. 43. Pattern-matching position and attitude residuals for generated test image: (a) x position; (b) y position; (c) z position; (d) pitch-plane angle; (e) yaw-plane angle; (f) roll angle.

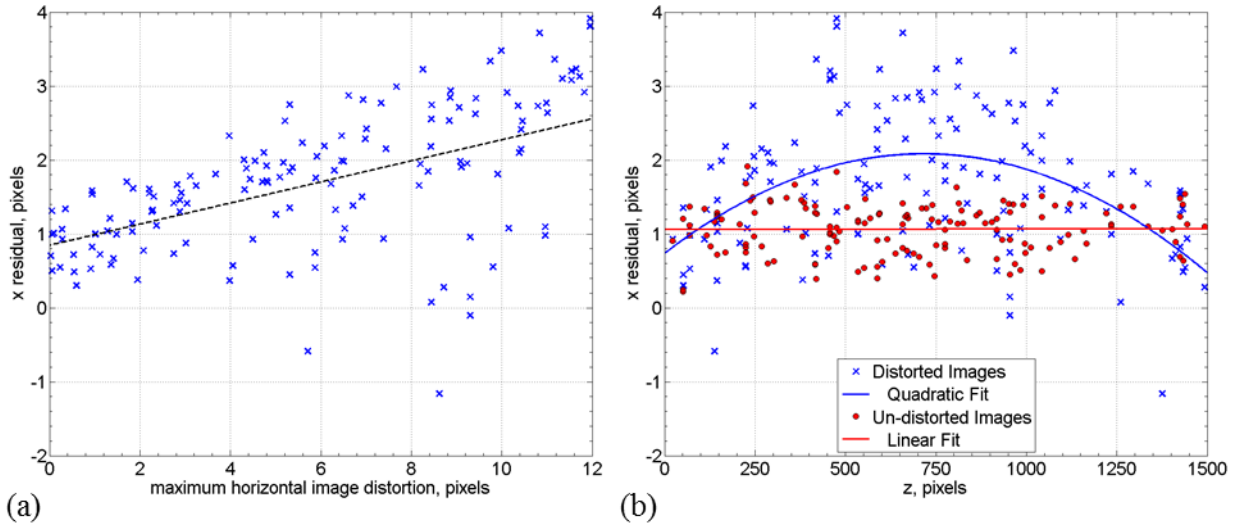

Fig. 44. x position residuals (a) as a function of degree of horizontal image distortion (curvature of the plumb wires), and (b) as a function of vertical (z) model position.